

Multipolar multiferroics in $4d^2/5d^2$ Mott insulators

Saikat Banerjee,^{1,2,*} Stephan Humeniuk,^{1,†} Alan R. Bishop,² Avadh Saxena,² and Alexander V. Balatsky^{3,4}

¹*Center for Materials Theory, Rutgers University, Piscataway, New Jersey, 08854, USA*

²*Theoretical Division, Los Alamos National Laboratory, Los Alamos, New Mexico 87545, USA*

³*Nordita, KTH Royal Institute of Technology and Stockholm University, 106 91 Stockholm, Sweden*

⁴*Department of Physics, University of Connecticut, Storrs, Connecticut 06269, USA*

(Dated: September 2, 2024)

We generalize conventional multiferroicity – simultaneous existence of ferroelectric and ferromagnetic orders – to multipolar degrees of freedom, examining its emergence in a d^2 Mott insulator with strong spin-orbit and Hund’s couplings. Specifically, we investigate the origin of magnetic multipolar interactions in d^2 Mott insulators. In addition, we show that an admixture of quadrupolar and octupolar magnetic order simultaneously induces electrical quadrupolar and ferroelectric polarization. Our theoretical formalism extends the multiferroic framework to the higher-order sector, exploring the possibility of coexisting multipolar orders of the same and different ranks. We finally comment on some of the experimental signatures.

Introduction.— Materials that exhibit coexistence of magnetic and ferroelectric order, commonly known as multiferroics, open up a promising avenue for the mutual control of both magnetism and ferroelectricity. Although the research in multiferroics dates back to the 1950s [1], the recent advancements in theory, synthesis, and characterization techniques have significantly revived interest in these materials. Over the past two decades, many candidate materials have been experimentally identified to harbor coexisting (dipolar) multiferroic orders [2, 3]. Notably, there is a growing list of experimental evidence for materials exhibiting even multipolar (quadrupolar, octupolar, etc.) or the so-called hidden orders [4–7]. One such example is the long-standing puzzle of the hexadecapolar order arising in f -electron-based uranium ions responsible for the low-temperature phase transition in URu₂Si₂ [8], which is typically accompanied by various higher-order charge (or polar) multipoles [9]. Therefore, it is natural to build a theoretical framework for the microscopic origin of the simultaneous emergence of such multipolar orders and to look for their concomitant experimental signatures.

Traditionally, the multiferroic studies have been focused on the dipolar limits of the spin and charge degrees of freedom (DF) in materials ranging from metals and semiconductors to Mott insulators [10–16]. The charge DF is gapped for Mott insulators, which facilitates a low-energy spin-only description – typically leading to a magnetic order. In principle, a generic non-collinear spin texture in the magnetically ordered state can break inversion symmetry and allow for ferroelectric polarization in spin-orbital coupled transition metal (TM) compounds [7, 17–19]. This is known as the Katsura-Nagaosa-Balatsky (KNB) mechanism. Conversely, preformed ferroelectric polarization can induce magnetization in certain mixed-valence compounds, known as improper ferroelectrics [20, 21]. Additionally, orbital DF

can spontaneously induce magnetization and ferroelectric polarization in frustrated magnetic systems allowing for multiferroic responses [22–24].

From a broader viewpoint, multiferroics can be categorized into two main types: type I hosts coexisting electric and magnetic responses, albeit with minimal mutual coupling – such as in perovskites BaTiO₃ [25], Pb(ZrTi)O₃ [26], where the multiferroic properties stem from the crystal structure, in BiMn(Fe)O₃ [27] with lone-pair induced multiferroicity, or in LiFe₂F₆ [28] with charge ordering-induced ferroelectricity. On the other hand, type II multiferroics demonstrate a significant coupling between electric and magnetic responses, as in the KNB mechanism.

The complexity arises when the Mott insulator lacks (dipolar) spins in the low-energy description but is only governed by higher-order multipoles – a common scenario in heavy fermionic or TM compounds due to a subtle interplay of crystal field effects, spin-orbit coupling (SOC), and Hund’s coupling [29, 30]. In this case, the dipolar magnetic ordering is absent, and instead, there is a quadrupolar or an octupolar ordering [31–37]. This naturally leads to the question: can we expect an emergent ferroelectric polarization induced by such magnetic multipoles? In general, is there a potential scheme for cross-coupling between the magnetic and electric multipoles?

To address these questions, here, we consider d^2 Mott insulators in the presence of strong SOC and Hund’s couplings – which host magnetic multipolar (quadrupole and octupole) moments [32]. We revisit the microscopic details pertinent to d^2 -systems and derive the multipolar exchange Hamiltonian in an edge-shared octahedral geometry. Based on symmetry, we find the generic presence of a trilinear multipolar exchange term in a magnetic field. Utilizing classical Monte Carlo simulation, we observe that the competition of the bilinear and trilinear exchange terms can lead to a non-collinear multipolar texture within an extended parameter space [see Fig. 3(a)], and simultaneously allows for induced ferroelectric and ferro-quadrupolar charge responses in the presence of ligand sites. Without aiming for a quanti-

* saikat.banerjee@rutgers.edu

† stephan.humeniuk@gmail.com

TABLE I. A summary of the higher-order multiferroic couplings. Notation: $l = 1 \rightarrow$ dipolar, $l = 2 \rightarrow$ quadrupolar, $l = 3 \rightarrow$ octupolar etc., and $l_{E(M)} \rightarrow$ electrical (magnetic) sectors. The hetero-(homo)-geneous multiferroicity signifies coupling between different (same) order multipoles.

Conventional		Multipolar		
l_E	l_M	Type	l_E	l_M
-	-	Heterogeneous	1	3
1	1	Homogeneous	2	2
Ref. [13, 17]		This work		

tative theory, we nevertheless translate our results into realistic estimates relevant to the materials of interest. Importantly, we extend the multiferroic paradigm beyond conventional dipole-dipole coupling and open avenues for further investigations into multipolar sectors. Some possible experimental signatures and diagnostics are also discussed.

Multipolar multiferroic framework.— Here, we present a simplified mathematical framework for the possible multipolar multiferroic coupling in Mott insulators. We adopt a convention in which the “atomic” low-energy DF are characterized by the Stevens operators \mathcal{O}_{lm} [38]. The lowest-order Stevens operators are nothing but the spin DF [30]. However, for complex multiorbital systems, the effective low-energy model can be described by higher-order Stevens operators, leading to an effective low-energy multipolar exchange model. Such higher-order exchange interactions favor interesting multipolar (quadrupolar, octupolar, etc.) ordering in the parent Mott insulator [2, 32–36, 39].

In contrast, the charge DF are gapped within a Mott insulator. Therefore, the electric multipole moments can be induced only via the virtual exchange processes of the electrons in the absence of doping. For a discrete charge distribution $\rho(\mathbf{r}_i)$, such multipole moments are defined as

$$\mathcal{Q}_{lm} = e \sum_{i=1}^N \int Z_{lm}^*(\delta\mathbf{r}_i) \delta\mathbf{r}_i^l \psi_f^*(\delta\mathbf{r}_i) \psi_i(\delta\mathbf{r}_i) d^3\mathbf{r}, \quad (1)$$

where $Z_{lm}(\delta\mathbf{r}_i) = \sqrt{\frac{4\pi}{2l+1}} Y_{lm}(\delta\mathbf{r}_i)$ are the spherical harmonics with Racah normalization, $\delta\mathbf{r}_i = \mathbf{r} - \mathbf{r}_i$, N is the number of sites in a finite-size cluster, and $\psi_{f,i}$ are the initial and final states. Subsequently, we adopt the real representation of \mathcal{Q}_{lm} by constructing the tesseral harmonics (which are certain types of spherical harmonics) as [38]

$$\mathcal{Q}_{lm}^c = (-1)^m \frac{\mathcal{Q}_{lm} + \mathcal{Q}_{lm}^*}{\sqrt{2}}, \quad \mathcal{Q}_{lm}^s = (-1)^m \frac{\mathcal{Q}_{lm} - \mathcal{Q}_{lm}^*}{\sqrt{2}i}. \quad (2)$$

Rewriting Eq. (1) in this way is beneficial as both the electric and magnetic multipolar moments transform identically under the point-group representations of the underlying crystal structure. Under two discrete

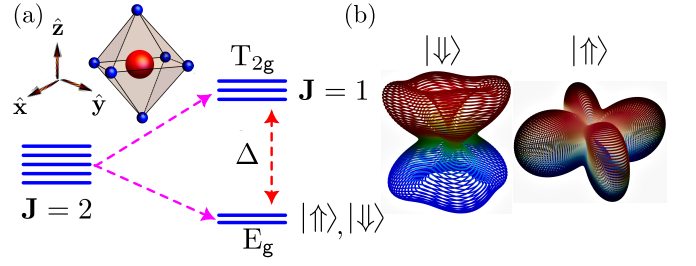


FIG. 1. (a) Left: Schematic of an octahedral unit-cell with TM atoms (red sphere) surrounded by the ligand (blue spheres). The crystal field further splits the $\mathbf{J} = 2$ states into an E_g doublet and a T_{2g} triplet. Right: The corresponding T_{2g} , and E_g splitting of $\mathbf{J} = 2$ atomic energy levels under the influence of crystal field ($\Delta_{\text{crys.}}$), Hund’s coupling (J_H) and SOC (λ). Here, Δ denotes a renormalized crystal field acting on the $\mathbf{J} = 2$ manifold. (b) The spatial distribution of the charge density for the pseudo-spin up and down states. The spatial shapes of the E_g doublet are inequivalent compared to the conventional Kramer’s doublets.

symmetries: parity/inversion (\mathcal{P}) and time-reversal (\mathcal{T}), the corresponding multipolar moments transform under these two symmetries as $\mathcal{P} : \mathcal{Q}_{lm}^{c/s} \rightarrow (-1)^l \mathcal{Q}_{lm}^{c/s}$, and $\mathcal{T} : \mathcal{O}_{lm} \rightarrow (-1)^l \mathcal{O}_{lm}$. Since they transform identically, the obvious possibility is whether a certain configuration of magnetic multipolar moments can trigger multipolar charge responses and vice versa. It can be considered a higher-order generalization of the KNB mechanism for the type II multiferroics [17, 22, 24] as illustrated in Table I.

Model.— We start from three higher-order magnetic Stevens operators, namely $\mathcal{O}_{20} = 3J_z^2 - \mathbf{J}^2$, $\mathcal{O}_{22} = J_x^2 - J_y^2$, and $\mathcal{T}_{xyz} = \overline{J_x J_y J_z}$ (average corresponds to symmetrization over all indices). They emerge as the low-energy effective DF in d^2/f^2 Mott insulators with strong SOC and Hund’s coupling [4, 31, 32, 34, 35]. For a d^2 ion in an octahedral crystal field, the atomic ground state is the non-Kramer’s E_g doublet characterized by the total angular momentum operator $\mathbf{J} = \mathbf{L} + \mathbf{S}$ [32]. The corresponding atomic energy splitting is illustrated in Fig. 1, with the E_g states given by

$$|\uparrow\rangle = \frac{1}{\sqrt{2}}(|J_z = 2\rangle + |J_z = -2\rangle), \quad |\downarrow\rangle = |J_z = 0\rangle. \quad (3)$$

The detailed spatial structure of these states with two spin-orbit coupled d -electrons in the crystal field splitting is given in the Supplementary Material (SM) [40]. The real-space charge distribution for the pseudo-spin states is shown in Fig. 1(b). We notice that the $|\uparrow\rangle$ -state is distributed along the xy -plane since one of the electrons has to occupy a d_{xy} orbital, while the $|\downarrow\rangle$ -state is elongated along the z -axis as two electrons can simultaneously occupy the d_{yz} , and d_{zx} orbitals [40]. Normalizing the Stevens operators as follows

$$\frac{\mathcal{O}_{22}}{4\sqrt{3}} \rightarrow \tilde{\sigma}^x, \quad \frac{\mathcal{T}_{xyz}}{2\sqrt{3}} \rightarrow \tilde{\sigma}^y, \quad \frac{\mathcal{O}_{20}}{12} \rightarrow \tilde{\sigma}^z, \quad (4)$$

it can be shown that they satisfy an effective SU(2) pseudo-spin algebra within the E_g subspace, *i.e.*, $[\tilde{\sigma}^\alpha, \tilde{\sigma}^\beta] = i\epsilon_{\alpha\beta\gamma}\tilde{\sigma}^\gamma$.

In the presence of inter-site hopping, we can obtain the effective multipolar exchange interaction by performing perturbation theory on the original Hubbard-Kanamori model. Ignoring Jahn-Teller distortions, we consider an ideal edge-sharing octahedral geometry as shown in Fig. 2(a), and focus within the [111] plane, where the TM sites form a honeycomb lattice [32]. We integrate out the ligand DF and consider only the direct hopping between the TM sites – leading to a bond-dependent multi-orbital hopping between the three t_{2g} orbitals: d_{xy} , d_{yz} , & d_{zx} . Assuming finite nearest- and next-nearest neighbor hoppings, we perform a Schrieffer-Wolff transformation (SWT) [41].

At first, we note that under time-reversal symmetry (TRS) transformation, pseudo-spin operators transform as $\mathcal{T} : \{\tilde{\sigma}^x, \tilde{\sigma}^y, \tilde{\sigma}^z\} \rightarrow \{\tilde{\sigma}^x, -\tilde{\sigma}^y, \tilde{\sigma}^z\}$, as evident from Eq. (4). This fact constrains the possible bilinear and trilinear exchange terms. For example, terms including a single $\tilde{\sigma}^y$ like $\tilde{\sigma}_i^\eta \tilde{\sigma}_j^\eta$ ($\eta = x, z$) are not allowed in the bilinear exchange. Furthermore, the trilinear exchange may contain terms like $\tilde{\sigma}_i^y \tilde{\sigma}_j^y \tilde{\sigma}_k^{x/z}$, and any other combinations. However, such terms would be forbidden by C_3 symmetry. Here, i, j, k correspond to site indices on the smallest possible loops in the honeycomb lattice. Additionally, we notice that $\tilde{\sigma}^x$ and $\tilde{\sigma}^z$ transform like a conventional e_g orbital in the Kugel-Khomskii model [42]. Considering Γ_3 symmetry [43, 44], we define the pseudo-spin combination along three different bonds as $\tau^\eta = \cos\phi_\eta \tilde{\sigma}^z + \sin\phi_\eta \tilde{\sigma}^x$, and $\bar{\tau}^\eta = -\sin\phi_\eta \tilde{\sigma}^z + \cos\phi_\eta \tilde{\sigma}^x$ where $\phi_\eta = (0, \frac{2\pi}{3}, \frac{4\pi}{3})$ along $\eta = z, x, y$ bond directions. Note that $\tilde{\sigma}^y$ remains invariant under the cubic $C_3^{[111]}$ rotation.

The microscopic Hamiltonian is given by $\mathcal{H} = \mathcal{H}_0 + \mathcal{H}_1$, where

$$\begin{aligned} \mathcal{H}_0 &= U \sum_{i\alpha} n_{i\alpha\uparrow} n_{i\alpha\downarrow} + \frac{U'}{2} \sum_{i,\alpha\neq\beta} n_{i\alpha\sigma} n_{i\beta\sigma'} + \Delta_{\text{crys.}} \sum_{i,\sigma} n_{i\sigma}^p + \\ &- \frac{J_H}{2} \sum_{i,\alpha\neq\beta} d_{i\alpha\sigma}^\dagger d_{i\alpha\sigma'} d_{i\beta\sigma}^\dagger d_{i\beta\sigma'} + \lambda \sum_{i,\alpha\beta} d_{i\alpha\sigma}^\dagger (\mathbf{L} \cdot \mathbf{S})_{\alpha\beta} d_{i\beta\sigma'}, \\ \mathcal{H}_1 &= \sum_{ij,\eta} t_{\alpha\beta}^{(\eta)} d_{i\alpha\sigma}^\dagger d_{j\beta\sigma'} + t_{pd}^{(\eta)} \sum_{\langle il \rangle, \eta} p_{l\sigma}^\dagger d_{i\alpha\sigma} + \text{h.c.}, \end{aligned} \quad (5)$$

where U , U' denote the intra- and inter-orbital Coulomb repulsion and J_H is the Hund's coupling. Here $\Delta_{\text{crys.}}$ denotes the ligand charge-transfer energy, λ is the strength of the SOC, and $t_{\alpha\beta}^{(\eta)}$, $t_{\alpha\beta}'^{(\eta)}$ ($t_{pd}^{(\eta)}$) correspond to the various bond-dependent TM-TM (TM-ligand) hopping amplitudes as shown in Fig. 2(b,c). For simplicity, we integrate out the ligand degrees of freedom and consider a renormalized nearest-neighbor TM-TM hopping as $t_{\alpha\beta}^{(\eta)} \rightarrow t_{\alpha\beta}^{(\eta)} + (t_{pd}^{(\eta)})^2 / \Delta_{\text{crys.}}$ [45], with $t_{\alpha\beta}^{(\eta)}$ obtained via Slater-Koster integrals [46]. Projecting the microscopic Hamiltonian in Eq. (5) into the E_g doublet, we

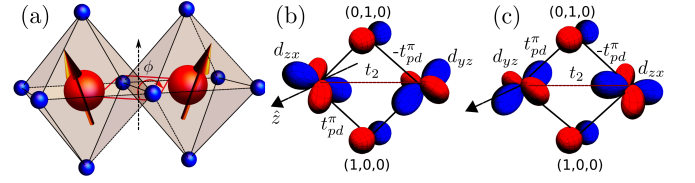


FIG. 2. (a) Edge-sharing octahedral geometry for TM-ligand compounds – the red spheres represent the TM ions, and the smaller blue spheres represent the ligands. Here, we do not consider any deviations from $\phi = 90^\circ$. Arrows signify a generic non-collinear orientation of the classical ground states in terms of pseudo-spin vectors $\{\tilde{\sigma}^x, \tilde{\sigma}^y, \tilde{\sigma}^z\}$. Panels (b) and (c) show the hopping channels for the z -bond mediated by the p orbitals of ligand atoms. Note that only d_{yz} and d_{zx} orbitals can hop via the ligand p_z orbitals at $(1,0,0)$ and $(0,1,0)$, respectively. In addition, only the upper and lower hopping paths in (b) and (c) provide non-vanishing contributions.

obtain the effective multipolar exchange Hamiltonian as $\mathcal{H} = \sum_\eta \mathcal{H}_\eta + \mathcal{H}_{xyz}$ where

$$\mathcal{H}_\eta = J^{(2)} \sum_{\langle ij \rangle, \eta} (\tilde{\sigma}_i^y \tilde{\sigma}_j^y - \tilde{\sigma}_i^x \tilde{\sigma}_j^x - \tilde{\sigma}_i^z \tilde{\sigma}_j^z). \quad (6)$$

Note the bilinear exchange interaction is identical along all the bond directions $\eta \in \{x, y, z\}$. This is consistent with the cubic rotation symmetry of the pseudo-spin DF [32]. The energy scale of the bilinear exchange term is $J^{(2)} = \frac{2t_2^2}{3\Delta E_{\text{ex.}}}$, where $\Delta E_{\text{ex.}} = U - 3J_H + \lambda$. Based on the requirement that the Hamiltonian needs to be C_3 -symmetric and even under TRS, and the octupolar component $\tilde{\sigma}^y$ is odd under TRS, the following trilinear part \mathcal{H}_{xyz} is allowed by symmetry only in the presence of an external magnetic field. The latter reads as

$$\mathcal{H}_{xyz} = \chi_s \sum_{\langle\langle ijk \rangle\rangle} (\alpha \tilde{\sigma}_i^x \tilde{\sigma}_j^x + \alpha \tilde{\sigma}_i^z \tilde{\sigma}_j^z - \beta \tilde{\sigma}_i^y \tilde{\sigma}_j^y) \tilde{\sigma}_k^y + P_{ijk}, \quad (7)$$

where $\langle\langle ijk \rangle\rangle$ denotes all possible triangles of nearest-neighbor sites on the honeycomb lattice, P_{ijk} indicates the cyclic permutations of the site indices i, j, k , and $\chi_s = \frac{2t_2^2 t_2'}{3\Delta E_{\text{ex.}}} \sin \frac{e\Phi}{hc}$, with Φ being the total flux in the triangular plaquette in an external magnetic field (B) [47]. Here, we ignored the virtual hopping between T_{2g} and E_g sectors and truncated the SWT expansion to the linear order in B . For the phenomenological coefficients we choose $\alpha = \frac{2}{9}$, $\beta = \frac{1}{9}$.

Multipolar ordering. – We use Monte Carlo simulations to elucidate the phase diagram of the multipolar exchange Hamiltonian in a magnetic field and the possibility of non-collinear spin textures as we tune the relative strength of the bilinear and trilinear [Eqs. (6),(7)] terms. We label this parameter as $\zeta = \chi_s / J^{(2)} = t_2' / \Delta E_{\text{ex.}} \sin \frac{e\Phi}{hc}$. We adopt a classical approximation as $\tilde{\sigma}_i = (\sin\theta_i \cos\phi_i, \sin\theta_i \sin\phi_i, \cos\theta_i)$, where we assume each pseudo-spin to be an O(3) vector satisfying $|\tilde{\sigma}_i \cdot \tilde{\sigma}_i| = 1$. The simulations are performed using the standard Metropolis single-spin flip update [48] and parallel

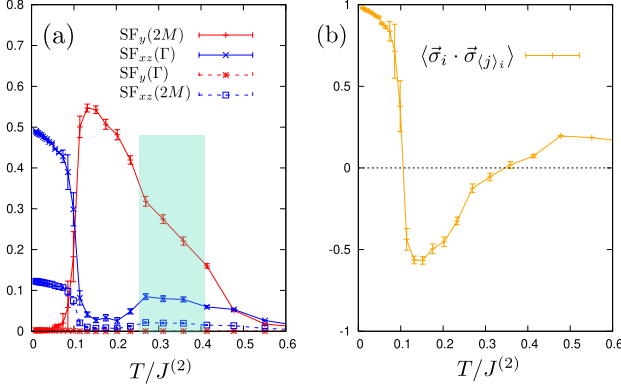


FIG. 3. (a) Structure factor of the octupolar (SF_y) and quadrupolar (SF_{xz}) spin components at momentum points Γ and $2M$. The strength of the three-spin term is $\zeta = 0.15$ and the system size is $12 \times 12 \times 2$. For $T/J^{(2)} < 0.1$, the order is quadrupolar (xz) FM, whereas for $0.1 < T/J^{(2)} < 0.5$ it is octupolar (y) AFM. In the shaded region the spin configuration is canted, i.e. (y) AFM and (xz) FM orders coexist. (b) Average dot product between neighboring spins as a crude measure of collinearity.

tempering [49] with a geometric temperature grid. Without a three-spin term ($\zeta = 0$), the bilinear Hamiltonian of Eq. (6) can be brought to the form of a Heisenberg antiferromagnet by the gauge transformation $\tilde{\sigma}_i^{x,z} \rightarrow -\tilde{\sigma}_i^{x,z}$, which is a rotation by π around the y -quantization axis, on one of the two sublattices, and the ground state is a Néel antiferromagnet. In the original spin variables this corresponds to antiferromagnetically (AFM) aligned octupolar (y) components and ferromagnetically (FM) aligned quadrupolar (xz) components of equal strength.

As Fig. 3(a) shows, the three-spin term Eq. (7) changes the balance between octupolar and quadrupolar components: The ground state and low-temperature phase is quadrupolar (xz) FM, which is separated by a sharp spin-flop transition from a phase which is predominantly octupolar (y) AFM. This is evidenced by the structure factor for the quadrupolar components, $SF_{xz}(\mathbf{q}) = \frac{1}{N^2} \sum_{ij} e^{i\mathbf{q} \cdot (\mathbf{r}_i - \mathbf{r}_j)} \langle \frac{1}{2} (\tilde{\sigma}_i^x \tilde{\sigma}_j^x + \tilde{\sigma}_i^z \tilde{\sigma}_j^z) \rangle$, and octupolar component, $SF_y(\mathbf{q}) = \frac{1}{N^2} \sum_{ij} e^{i\mathbf{q} \cdot (\mathbf{r}_i - \mathbf{r}_j)} \langle \tilde{\sigma}_i^y \tilde{\sigma}_j^y \rangle$: In the xz -FM phase $SF_{xz}(\tilde{q})$ has a peak at the center of the first Brillouin zone $\mathbf{q} = \Gamma = (0, 0)$ and a second peak of 1/4 of its strength at the point $\mathbf{q} = 2M = (\frac{2\pi}{a}, \frac{2\pi}{\sqrt{3}a})$ at the center of the second Brillouin zone, which indicates intra-unit-cell order. Here a is the lattice constant of the triangular Bravais lattice underlying the honeycomb structure. By contrast, in the y -AFM phase $SF_y(2M)$ is large and $SF_y(\Gamma)$ vanishes. Importantly, there is a finite-temperature window where both $SF_y(2M)$ and $SF_{xz}(\Gamma)$ are non-zero and of unequal strength, which indicates a non-collinear, canted spin configuration that is AFM in y -components and FM in xz -components. This region is shaded in Fig. 3(a). As a crude measure of collinearity we consider the dot product between nearest neighbor

spins, $\langle \tilde{\sigma}_i \cdot \tilde{\sigma}_{(j)_i} \rangle$, averaged over all bonds $(i, (j)_i)$, which is shown in Fig. 3(b) and is consistent with a quadrupolar FM polarized low-temperature state and an octupolar AFM or canted state at intermediate temperature.

Ferroelectric polarization.— First, we model the possible non-collinear texture that follows from the multipolar exchange Hamiltonian in Eqs. (6), and (7) by a local approximation as $\mathcal{H}_{\text{local}} = -\tilde{U} \sum_i \hat{e}_i \cdot \tilde{\sigma}_i$, where \tilde{U} denotes the local excitation energy, and $\hat{e}_i = (\cos \phi_i \sin \theta_i, \sin \phi_i \sin \theta_i, \cos \theta_i)$ describes the multipolar moments at site i [17]. Next, we consider a four-site cluster of two TM and two ligand atoms in the edge-shared geometry as shown in Fig. 2(a), and furthermore consider *filled* ligand sites. Subsequently, we allow ligand-TM charge transfer processes in a double-exchange (DE) framework and consider two different hopping paths ($t_{pd}^\pi > 0$) in the upper and lower triangular plaquettes as in Fig. 2(b). The eigenstates are obtained by diagonalizing $\mathcal{H}_{\text{local}}$ as follows

$$\begin{aligned} |\psi^+\rangle &= \cos \frac{\theta_i}{2} |\uparrow\uparrow\rangle + e^{i\phi_i} \sin \frac{\theta_i}{2} |\downarrow\downarrow\rangle, \\ |\psi^-\rangle &= \sin \frac{\theta_i}{2} |\uparrow\uparrow\rangle - e^{i\phi_i} \cos \frac{\theta_i}{2} |\downarrow\downarrow\rangle, \end{aligned} \quad (8)$$

where $|\uparrow\rangle, |\downarrow\rangle$ are the same as in Eq. (3), with energies $\mp \tilde{U}$. Assuming a finite TM-ligand hopping (t_{pd}), we compute the perturbation correction to the ground states in Eq. (8) leading to an intermediate configuration: d^3, p_z^1 . Furthermore, we consider strong Hund's coupling for the d^3 configuration in the octahedral crystal field. Utilizing the explicit form of these perturbed states $|\psi\rangle$ in the four-site cluster (see the details in the SM [40]), we analyze the expectation value of the ferroelectric polarization $\mathbf{P} = \langle \psi | \mathbf{er} | \psi \rangle$. We notice that for the z -bond, only the x -component of \mathbf{P} is finite and is given by

$$\langle P_x \rangle \approx \frac{eIt_{pd}^\pi}{3\Delta_{\text{crys}}} \cos \frac{\theta_i}{2} \cos \frac{\theta_j}{2} \sin(\phi_i - \phi_j), \quad (9)$$

where I is the overlap integral given as $\int d\mathbf{r} d_{i,r}^{xy} d_{i,r}^{yz} x p_{i,r}^z d_{j,r}^{xy} d_{j,r}^{yz} d_{j,r}^{zx}$ and its cyclic permutations. Note that the emergent polarization is odd under inversion symmetry (which is broken within the non-collinear multipolar texture) and is bond-dependent. For other bonds, the finite component is obtained by cyclic permutation of x, y, z . We further note that without any octupolar component, i.e. $\phi_i = 0$, the polarization vanishes – consistent with our earlier phenomenological analysis (see Table I, heterogeneous type: $l_E = 1, l_M = 3$). This result can be considered a multipolar generalization of the KNB mechanism [17] for spin current-induced ferroelectricity in generic non-collinear magnets.

Electrical quadrupole.— Assuming the same four-site geometry as before (see Fig. 2), here we shift our focus to charge transfer between TM and *empty* ligand sites. We now consider a cotunneling mechanism, where each electron from the TM sites hops simultaneously to the empty ligand sites, as illustrated in Fig. 2(c). Physically, this process is extremely unlikely but possible in principle.

To study this cotunneling process and its implications for the electronic structure, we employ a similar perturbative approach as before and focus on the correction to the ground state in Eq. (8) leading to the intermediate configuration: d^0, p_z^1, p_z^1 . Again utilizing the perturbed states $|\psi\rangle$ within the four-site cluster (see the details in the SM [40]), we analyze the expectation value of the electrical multipole moment \mathcal{Q}_{lm} as defined in Eq. (2). In line with our local approximation to the exchange Hamiltonian, we find that for the z -bond only \mathcal{Q}_{21}^s and \mathcal{Q}_{22}^s are non-vanishing. Setting the origin at the center of the cluster, we obtain

$$\mathcal{Q}_{21}^s \approx \frac{8eI'(t_{pd}^\pi)^2}{3\sqrt{3}\Delta_{\text{crys}}^2} \cos \frac{\theta_i}{2} \cos \frac{\theta_j}{2} \cos(\phi_i - \phi_j), \quad (10a)$$

$$\mathcal{Q}_{22}^s \approx \frac{4eI'(t_{pd}^\pi)^2}{3\Delta_{\text{crys}}^2} \cos \frac{\theta_i}{2} \sin \frac{\theta_j}{2} \cos \phi_i + i \leftrightarrow j + \mathcal{Q}_{21}^s, \quad (10b)$$

where I' is the overlap integral given as $\int d\mathbf{r} d_{i,\mathbf{r}}^{xy} d_{i,\mathbf{r}}^{zx} p_{i,\mathbf{r}}^z p_{i,\mathbf{r}}^z$, and its cyclic permutations. Here, l' corresponds to the position of the two ligand atoms in the upper and lower triangles in Fig. 2(c). For other bonds, the non-vanishing quadrupolar components can be obtained by cyclic permutations of x, y, z . Note that, even without any magnetic octupolar moments, the electrical quadrupolar moment survives and arises purely from the magnetic quadrupole, consistent with Table I, homogeneous type: $l_E = 2, l_M = 2$.

Experimental signatures.— Our proposal can potentially be realized in a wide class of $4d^2/5d^2$ Mott insulators with an edge-sharing octahedral geometry. A typical example would be the Os^{6+} or Re^{5+} ion in this configuration. The presence of multipolar ordering can be indirectly observed using two successive techniques: the absence of any sharp feature in neutron scattering (which rules out long-range magnetic ordering) and the observation of a phase transition in specific heat measurements. Additionally, ferroelectric polarization can be confirmed by optical second harmonic generation, which would otherwise be absent in a centrosymmetric system [50]. While

characterizing the electrical quadrupolar moment is challenging, by virtue of selection rules the two-photon absorption technique could, in principle, be used to detect its presence in candidate materials [51]. Another way of detecting multipolar multiferroic order is through the measurements of higher order magnetoelectric coefficients.

Discussion and conclusion.— In this Letter, we proposed a theoretical formalism to generalize conventional multiferroicity – coupling between ferromagnetic and ferroelectric response – to higher-order sectors. We showed that magnetic quadrupolar and octupolar moments in a strong Hund's and spin-orbit coupled d^2 Mott insulator can induce dipolar and quadrupolar charge distribution in the presence of ligand degrees of freedom. Specifically, the multipolar exchange Hamiltonian was explicitly derived for edge-shared octahedral compounds using the low-energy atomic E_g states. Utilizing classical Monte Carlo simulation, we find indication that the bilinear and trilinear exchange Hamiltonian for a d^2 -Mott insulator in a magnetic field can host a canted pseudo-spin configuration, thereby realizing the scenario of non-collinear multipolar order. And finally, we show that a non-collinear magnetic octupolar order induces ferroelectric polarization, while a non-collinear magnetic quadrupolar order hosts a quadrupolar charge distribution.

Acknowledgments.— We acknowledge helpful discussions with Giniyat Khaliullin, Hosho Katsura, and Niels Grønbech-Jensen. S.B. is grateful to the Department of Physics, University of Connecticut, Storrs, USA, for hosting, where part of the work was initiated. The work in Los Alamos was carried out under the auspices of the U.S. Department of Energy (DOE), Office of Science, and Office of Advanced Scientific Computing Research through the Quantum Internet to Accelerate Scientific Discovery Program. We gratefully acknowledge partial support from the Office of Basic Energy Sciences, Material Sciences and Engineering Division, U.S. DOE, under Contract No. DE-FG02-99ER45790. Computations were performed on the cluster of the Center for Materials Theory at the Department of Physics and Astronomy at Rutgers University.

-
- [1] W. Windsch, A. J. Freeman, H. Schmid. Magnetoelectric interaction phenomena in crystals. Gordon and Breach Science Publishers London 1975. £ 10.90, *Krist. Tech.* **11**, K45 (1976).
- [2] Y.-D. Li, X. Wang, and G. Chen, Hidden multipolar orders of dipole-octupole doublets on a triangular lattice, *Phys. Rev. B* **94**, 201114 (R) (2016).
- [3] R. M. Fernandes, P. P. Orth, and J. Schmalian, Intertwined Vestigial Order in Quantum Materials: Nematicity and Beyond, *Annu. Rev. Condens. Matter Phys.* **10**, 133 (2019).
- [4] A. S. Patri, A. Sakai, S. Lee, A. Paramakanti, S. Nakatsuji, and Y. B. Kim, Unveiling hidden multipolar orders with magnetostriction, *Nat. Commun.* **10**, 4092 (2019).
- [5] D. Hirai, H. Sagayama, S. Gao, H. Ohsumi, G. Chen, T.-h. Arima, and Z. Hiroi, Detection of multipolar orders in the spin-orbit-coupled $5d$ Mott insulator $\text{Ba}_2\text{MgReO}_6$, *Phys. Rev. Res.* **2**, 022063 (2020).
- [6] P. Santini, S. Carretta, G. Amoretti, R. Caciuffo, N. Magnani, and G. H. Lander, Multipolar interactions in f -electron systems: The paradigm of actinide dioxides, *Rev. Mod. Phys.* **81**, 807 (2009).
- [7] G. Aeppli, A. V. Balatsky, H. M. Rønnow, and N. A. Spaldin, Hidden, entangled and resonating order, *Nat. Rev. Mater.* **5**, 477 (2020).
- [8] K. Haule and G. Kotliar, Arrested Kondo effect and hidden order in URu_2Si_2 , *Nat. Phys.* **5**, 796 (2009).
- [9] J. Mydosh and P. Oppeneer, Hidden order behaviour in

- URu₂Si₂ (A critical review of the status of hidden order in 2014), *Phil. Mag.* **94**, 3642 (2014).
- [10] M. Fiebig, Revival of the magnetoelectric effect, *J. Phys. D: Appl. Phys.* **38**, R123 (2005).
- [11] W. Eerenstein, N. D. Mathur, and J. F. Scott, Multiferroic and magnetoelectric materials, *Nature* **442**, 759 (2006).
- [12] R. Ramesh and N. A. Spaldin, Multiferroics: progress and prospects in thin films, *Nat. Mater.* **6**, 21 (2007).
- [13] S.-W. Cheong and M. Mostovoy, Multiferroics: a magnetic twist for ferroelectricity, *Nat. Mater.* **6**, 13 (2007).
- [14] D. Khomskii, Classifying multiferroics: Mechanisms and effects, *Physics* **2**, 20 (2009).
- [15] S. Dong, H. Xiang, and E. Dagotto, Magnetoelectricity in multiferroics: a theoretical perspective, *Natl. Sci. Rev.* **6**, 629 (2019).
- [16] T. Lottermoser and D. Meier, A short history of multiferroics, *Phys. Sci. Rev.* **6**, 2020 (2021).
- [17] H. Katsura, N. Nagaosa, and A. V. Balatsky, Spin Current and Magnetoelectric Effect in Noncollinear Magnets, *Phys. Rev. Lett.* **95**, 057205 (2005).
- [18] Y. Tokura, S. Seki, and N. Nagaosa, Multiferroics of spin origin, *Rep. Prog. Phys.* **77**, 076501 (2014).
- [19] D. Bossini, D. M. Juraschek, R. M. Geilhufe, N. Nagaosa, A. V. Balatsky, M. Milanović, V. V. Srdčić, P. Šenjug, E. Topić, D. Barišić, M. Rubčić, D. Pajić, T. Arima, M. Savoini, S. L. Johnson, C. S. Davies, and A. Kirilyuk, Magnetoelectrics and multiferroics: theory, synthesis, characterisation, preliminary results and perspectives for all-optical manipulations, *J. Phys. D: Appl. Phys.* **56**, 273001 (2023).
- [20] L.-F. Lin, Q.-R. Xu, Y. Zhang, J.-J. Zhang, Y.-P. Liang, and S. Dong, Ferroelectric ferrimagnetic LiFe₂F₆: Charge-ordering-mediated magnetoelectricity, *Phys. Rev. Mater.* **1**, 071401(R) (2017).
- [21] C. Ederer and N. A. Spaldin, A new route to magnetic ferroelectrics, *Nat. Mater.* **3**, 849 (2004).
- [22] L. N. Bulaevskii, C. D. Batista, M. V. Mostovoy, and D. I. Khomskii, Electronic orbital currents and polarization in Mott insulators, *Phys. Rev. B* **78**, 024402 (2008).
- [23] S. Banerjee and S.-Z. Lin, Emergent orbital magnetization in Kitaev quantum magnets, *SciPost Phys.* **14**, 127 (2023).
- [24] S. Banerjee, W. Zhu, and S.-Z. Lin, Electromagnetic signatures of a chiral quantum spin liquid, *npj Quantum Mater.* **8**, 63 (2023).
- [25] R. Mangalam, N. Ray, U. V. Waghmare, A. Sundaresan, and C. Rao, Multiferroic properties of nanocrystalline batio₃, *Solid State Commun.* **149**, 1 (2009).
- [26] D. M. Evans, M. Alexe, A. Schilling, A. Kumar, D. Sanchez, N. Ortega, R. S. Katiyar, J. F. Scott, and J. M. Gregg, The Nature of Magnetoelectric Coupling in Pb(Zr,Ti)O₃-Pb(Fe,Ta)O₃, *Adv. Mater.* **27**, 6068 (2015).
- [27] A. A. Belik, Local distortions in multiferroic bmn₃ as a function of doping, *Sci. Technol. Adv. Mater.* **12**, 044610 (2011).
- [28] L.-F. Lin, Q.-R. Xu, Y. Zhang, J.-J. Zhang, Y.-P. Liang, and S. Dong, Ferroelectric ferrimagnetic LiFe₂F₆: Charge-ordering-mediated magnetoelectricity, *Phys. Rev. Mater.* **1**, 071401 (2017).
- [29] W. Witczak-Krempa, G. Chen, Y. B. Kim, and L. Balents, Correlated Quantum Phenomena in the Strong Spin-Orbit Regime, *Ann. Rev. Condens. Matter Phys.* **5**, 57 (2014).
- [30] T. Takayama, J. Chaloupka, A. Smerald, G. Khaliullin, and H. Takagi, Spin-Orbit-Entangled Electronic Phases in 4d and 5d Transition-Metal Compounds, *J. Phys. Soc. Japan* **90**, 062001 (2021).
- [31] G. Chen and L. Balents, Spin-orbit coupling in d^2 ordered double perovskites, *Phys. Rev. B* **84**, 094420 (2011).
- [32] G. Khaliullin, D. Churchill, P. P. Stavropoulos, and H.-Y. Kee, Exchange interactions, Jahn-Teller coupling, and multipole orders in pseudospin one-half $5d^2$ Mott insulators, *Phys. Rev. Res.* **3**, 033163 (2021).
- [33] A. Rayyan, D. Churchill, and H.-Y. Kee, Field-induced Kitaev multipolar liquid in spin-orbit coupled d^2 honeycomb Mott insulators, *Phys. Rev. B* **107**, L020408 (2023).
- [34] A. Paramekanti, D. D. Maharaj, and B. D. Gaulin, Octupolar order in d -orbital Mott insulators, *Phys. Rev. B* **101**, 054439 (2020).
- [35] D. D. Maharaj, G. Sala, M. B. Stone, E. Kermarrec, C. Ritter, F. Fauth, C. A. Marjerrison, J. E. Greedan, A. Paramekanti, and B. D. Gaulin, Octupolar versus Néel Order in Cubic $5d^2$ Double Perovskites, *Phys. Rev. Lett.* **124**, 087206 (2020).
- [36] S. Voleti, D. D. Maharaj, B. D. Gaulin, G. Luke, and A. Paramekanti, Multipolar magnetism in d -orbital systems: Crystal field levels, octupolar order, and orbital loop currents, *Phys. Rev. B* **101**, 155118 (2020).
- [37] D. Churchill and H.-Y. Kee, Competing multipolar orders in a face-centered cubic lattice: Application to the osmium double perovskites, *Phys. Rev. B* **105**, 014438 (2022).
- [38] H. Kusunose, Description of multipole in f -electron systems, *J. Phys. Soc. Japan* **77**, 064710 (2008).
- [39] L. V. Pourovskii, D. F. Mosca, and C. Franchini, Ferrooctupolar order and low-energy excitations in d^2 double perovskites of osmium, *Phys. Rev. Lett.* **127**, 237201 (2021).
- [40] See the Supplementary Material for more details.
- [41] S. Banerjee, U. Kumar, and S.-Z. Lin, Inverse Faraday effect in Mott insulators, *Phys. Rev. B* **105**, L180414 (2022).
- [42] K. I. Kugel' and D. I. Khomskii, The jahn-teller effect and magnetism: transition metal compounds, *Sov. Phys. Usp.* **25**, 231 (1982).
- [43] A. Abragam and B. Bleaney, *Electron Paramagnetic Resonance of Transition Ions*, International series of monographs on physics (Clarendon P., 1970).
- [44] G. Khaliullin, Orbital Order and Fluctuations in Mott Insulators, *Prog. Theor. Phys. Suppl.* **160**, 155 (2005).
- [45] A. Bolens, Theory of electronic magnetoelectric coupling in d^5 mott insulators, *Phys. Rev. B* **98**, 125135 (2018).
- [46] J. C. Slater and G. F. Koster, Simplified lcao method for the periodic potential problem, *Phys. Rev.* **94**, 1498 (1954).
- [47] D. Sen and R. Chitra, Large- u limit of a hubbard model in a magnetic field: Chiral spin interactions and paramagnetism, *Phys. Rev. B* **51**, 1922 (1995).
- [48] N. Metropolis, A. W. Rosenbluth, M. N. Rosenbluth, A. H. Teller, and E. Teller, Equation of State Calculations by Fast Computing Machines, *J. Chem. Phys.* **21**, 1087 (1953).
- [49] K. Hukushima and K. Nemoto, Exchange monte carlo method and application to spin glass simulations, *J. Phys. Soc. Jpn.* **65**, 1604 (1996).
- [50] F. Pavone and P. Campagnola, *Second Harmonic Generation Imaging*, Series in Cellular and Clinical Imaging

- (CRC Press, 2016).
- [51] H. Rabin and C. L. Tang, *Quantum electronics: a treatise. Volume I. Nonlinear optics, Part A* (Academic Press Inc., New York, United States, 1975).
 - [52] G. Khaliullin, Excitonic Magnetism in Van Vleck-type d^4 Mott Insulators, *Phys. Rev. Lett.* **111**, 197201 (2013).
 - [53] C. Svoboda, M. Randeria, and N. Trivedi, Effective magnetic interactions in spin-orbit coupled d^4 Mott insulators, *Phys. Rev. B* **95**, 014409 (2017).
 - [54] A. Georges, L. d. Medici, and J. Mravlje, Strong Correlations from Hund's Coupling, *Annu. Rev. Condens. Matter Phys.* **4**, 137 (2013).
 - [55] O. N. Meetei, O. Erten, M. Randeria, N. Trivedi, and P. Woodward, Theory of High T_c Ferrimagnetism in a Multiorbital Mott Insulator, *Phys. Rev. Lett.* **110**, 087203 (2013).
 - [56] U. Kumar, S. Banerjee, and S.-Z. Lin, Floquet engineering of Kitaev quantum magnets, *Commun. Phys.* **5**, 157 (2022).
 - [57] P. Hoffmann, Generalization of Stevens' operator-equivalent method, *J. Phys. A: Math. Gen.* **24**, 35 (1991).
 - [58] J. R. Schrieffer and P. A. Wolff, Relation between the Anderson and Kondo Hamiltonians, *Phys. Rev.* **149**, 491 (1966).
 - [59] A. B. Harris and R. V. Lange, Single-particle excitations in narrow energy bands, *Phys. Rev.* **157**, 295 (1967).
 - [60] J. G. Wright and B. S. Shastry, DiracQ: A Quantum Many-Body Physics Package, arXiv e-prints, arXiv:1301.4494 (2013).
 - [61] S. Han, D. J. Schultz, and Y. B. Kim, Non-Fermi liquid behavior and quantum criticality in cubic heavy fermion systems with non-Kramers multipolar local moments, *Phys. Rev. B* **106**, 155155 (2022).

Supplementary material – Multipolar multiferroics in $4d^2/5d^2$ Mott insulators

Saikat Banerjee,^{1,2,*} Stephan Humeniuk,^{1,†} Alan R. Bishop,² Avadh Saxena,² and Alexander V. Balatsky^{3,4}

¹ *Center for Materials Theory, Rutgers University, Piscataway, New Jersey, 08854, USA*

² *Theoretical Division, Los Alamos National Laboratory, Los Alamos, New Mexico 87545, USA*

³ *Nordita, KTH Royal Institute of Technology and Stockholm University, 106 91 Stockholm, Sweden*

⁴ *Department of Physics, University of Connecticut, Storrs, Connecticut 06269, USA*

(Dated: September 2, 2024)

CONTENTS

References	5
I. Introduction: Hubbard-Kanamori description	1
A. Energy manifold with strong SOC	2
B. Representation of the low-energy states	3
C. Clebsch-Gordon coefficients: Individual states	4
II. Schrieffer-Wolff transformation: Multipolar exchange Hamiltonian	4
A. Derivation of the low-energy effective exchange interaction	5
B. Second-order multipolar exchange interaction	6
C. Third-order multipolar exchange interaction	8
III. Multipolar multiferroicity	9
A. Ferroelectric polarization	9
B. Electrical quadrupolar distribution	10

I. INTRODUCTION: HUBBARD-KANAMORI DESCRIPTION

In this section, we delve into the specifics of the microscopic model Hamiltonian governing the behavior of transition metal (TM) compounds characterized by d^2 -electronic configurations. The comprehensive Hamiltonian indicated in the main text is expressed as follows

$$\mathcal{H} = \mathcal{H}_0 + \mathcal{H}_1 + \mathcal{H}_{\text{crys.}}, \quad (\text{S1a})$$

$$\mathcal{H}_0 = U \sum_{i\alpha} n_{i\alpha,\uparrow} n_{i\alpha,\downarrow} + \frac{U'}{2} \sum_{i,\alpha\neq\beta,\sigma,\sigma'} n_{i\alpha\sigma} n_{i\beta\sigma'} - \frac{J_H}{2} \sum_{\alpha\neq\beta,\sigma,\sigma'} d_{i\alpha\sigma}^\dagger d_{i\alpha\sigma'} d_{i\beta\sigma'}^\dagger d_{i\beta\sigma} + \lambda \sum_i d_{i\alpha\sigma}^\dagger (\mathbf{L}_{\alpha\beta} \cdot \mathbf{S}_{\sigma\sigma'}) d_{i\beta\sigma'}, \quad (\text{S1b})$$

$$\mathcal{H}_1 = \sum_{\substack{(ij) \\ \alpha\beta\sigma\sigma'}} t_{\alpha\beta;\sigma\sigma'} d_{i\alpha\sigma}^\dagger d_{j\beta\sigma'} + t_{pd} \sum_{\substack{i,l \\ \alpha\sigma}} p_{l\sigma}^\dagger d_{i\alpha\sigma} + \text{h.c.}, \quad (\text{S1c})$$

where (i) the indices α and β represent orbital indices, and they can take on values from the set $\{xy, yz, zx\}$, (ii) the σ term corresponds to the electronic spin degrees of freedom, (iii) U represents the strength of the onsite Coulomb repulsion, and (iv) J_H stands for Hund's coupling. In rotationally invariant systems, $U' = U - 2J_H$, (iv) λ denotes the strength of the atomic spin-orbit coupling (SOC), and (v) the operator p_σ^\dagger creates an electron at the ligand site with spin σ . In addition, a crystal field term $\mathcal{H}_{\text{crys.}}$, which accounts for the charge-transfer energy gap between the d - and p -sites, is introduced to the system as $\mathcal{H}_{\text{crys.}} = \Delta_{\text{crys.}} \sum_l p_{l\sigma}^\dagger p_{l\sigma}$. Here, $t_{\alpha\beta;\sigma\sigma'}$ characterizes the hopping amplitude between two TM sites, while t_{pd} represents the hopping amplitude between a TM site and a ligand site.

Before moving forward, we first analyze the onsite Hamiltonian \mathcal{H}_0 in detail to characterize the overall energy splitting. For this purpose, we strictly follow the following energy hierarchy as $U \gg \Delta_{\text{crys.}} \gg J_H \gtrsim \lambda$. Since there are two electrons in the d^2 -configuration, the total spin of the two-electron state is $\mathbf{S} = \mathbf{1}$. We consider a large crystal field in octahedral geometry, as shown in Fig. 1 in the main text. This leads to the conventional t_{2g} and e_g splitting of the isolated five degenerate d levels as shown in Fig. S1(b). However, because of the SOC the low-energy t_{2g} manifold further splits into total angular momentum $\mathbf{J} = (\mathbf{L} + \mathbf{S}) = 0, 1, 2$ sectors. Since the $\mathbf{J} = 2$ sector transforms under the

same symmetry as the original five d -levels, it can be shown that the effective renormalized crystal field further splits this low-energy $\mathbf{J} = 2$ manifold into yet another splitting. Considering the same terminology as in the previous case, we associate this to T_{2g} , and E_g levels [see Fig. S1(b) for an illustration] [S30]. Hence, the two-electron ground state is composed of a non-Kramers doublet labeled by E_g .

In an octahedral environment embedded in cubic geometry, we can formally write down the effective residual crystal field Hamiltonian as

$$\mathcal{H}_{\text{spl.}} = -\Delta (\mathcal{O}_{40} + 5\mathcal{O}_{44}), \quad (\text{S2})$$

where \mathcal{O}_{mn} are the Stevens operators [S34, S36] written in the J -basis as

$$\mathcal{O}_{40} = 35J_z^4 - [30J(J+1) - 25]J_z^2 + 3J^2(J+1)^2 - 6J(J+1), \quad (\text{S3a})$$

$$\mathcal{O}_{44} = \frac{1}{2} (J_+^4 + J_-^4), \quad (\text{S3b})$$

where $J_{\pm} = J_x \pm iJ_y$ are the raising and lowering operators, respectively, and Δ is the renormalized strength of the SOC-enabled crystal fields. Note that the octahedral group is a subgroup of the cubic group. Before moving forward, we first analyze the energy manifold constructed out of the two-electron states in the d^2 -Mott insulators.

A. Energy manifold with strong SOC

We consider a large crystal field compared to the parameters in the Hamiltonian in Eq. (S1b), subsequently leading to a large t_{2g} and e_g splitting in the d -orbital manifold. Therefore, in the d^2 -configuration, two electrons are forced to stay in the t_{2g} manifold, which is composed of three orbital angular momentum active orbitals: d_{xy} , d_{yz} , and d_{zx} . Since they are pointed orbitals and also form a cubic coordinate system, following Ref. [S52], we relabel them as $a \rightarrow d_{yz}$, $b \rightarrow d_{zx}$, and $c \rightarrow d_{xy}$. The two electrons reside in the t_{2g} manifold without any SOC. Therefore, there are three different configurations. Here, we consider $\Delta_{\text{crys}} > U \gg J_{\text{H}}, \lambda$. Hence, following the Hund's rule, we have

$$A = \{bc\}, B = \{ac\}, C = \{ab\}, \quad (\text{S4})$$

where we have ignored the spin degrees of freedom. As labeled above, the composite orbital configurations also form a cubic coordinate system. Writing out explicitly, we have

$$|\psi_{i;\alpha\beta,\sigma\sigma'}\rangle = d_{i;\alpha\sigma}^\dagger d_{i;\beta\sigma'}^\dagger |0\rangle, \quad \forall \alpha, \beta \in \{xy, yz, zx\}, \quad (\text{S5})$$

where $d_{i;\alpha,\sigma}^\dagger$ creates one electron at the site i with orbital α , and spin σ , and $|0\rangle$ corresponds to the empty t_{2g} manifold. There are ${}^6C_2 = 15$ possible configurations following Eq. (S5). To compute the energy, we use the simplified form for the Hubbard-Kanamori model (HKM) for the rotation invariant t_{2g} manifold as [S53, S54]

$$\mathcal{H}_0^{(i)} = (U - 3J_{\text{H}}) \frac{N_i(N_i - 1)}{2} + J_{\text{H}} \left(\frac{5}{2} N_i - 2S_i^2 - \frac{1}{2} L_i^2 \right), \quad (\text{S6})$$

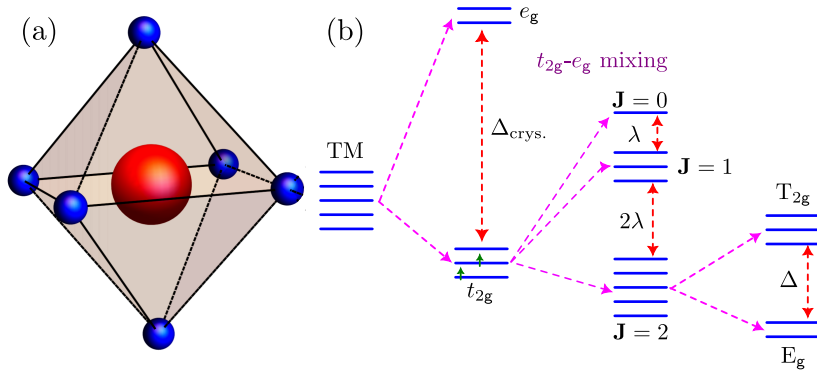


FIG. S1. (a) Schematic of the octahedral unit cell containing a central transition metal (TM) ion surrounded by six ligand sites. (b) Hierarchy of atomic onsite energy splitting for the five degenerate d -levels resulting from various interactions, as discussed in the text.

where N_i is electron number, S_i is total spin, and L_i is total orbital angular momentum. We include the SOC λ into the HKM. In this case, the spin and orbital angular momenta are entangled, and one needs to work in the total angular momentum basis as both \mathbf{L}_i and \mathbf{S}_i are not good quantum numbers anymore. The SOC part can be written as [S55]

$$\mathcal{H}_{\text{soc}}^{(i)} = \lambda \mathbf{L}_i \cdot \mathbf{S}_i = \frac{\lambda}{2} (\mathbf{J}_i^2 - \mathbf{L}_i^2 - \mathbf{S}_i^2), \quad (\text{S7})$$

where $\mathbf{J}_i = \mathbf{L}_i + \mathbf{S}_i$, with \mathbf{L}_i , and \mathbf{S}_i being the total orbital and spin angular momentum, respectively. In this case, the previous six-fold degeneracy is broken. We have a further splitting of t_{2g} manifold in $J = 0, 1, 2$ sub-manifolds, with the respective energies dictated by $\mathcal{H}_{\text{soc}}^{(i)}$ as: $E_{\text{soc}}^{(i)}|_{J=0} = -2\lambda$, $E_{\text{soc}}^{(i)}|_{J=1} = -\lambda$, and $E_{\text{soc}}^{(i)}|_{J=2} = \lambda$, where $J = 0$, $J = 1$, and $J = 2$ are singly, triply, and quintuply degenerate manifolds, respectively.

B. Representation of the low-energy states

At first, we define the orbital angular momentum operators on the basis of A, B, and C defined in Eq. (S6) as follows [S52]

$$L_x^{(i)} = -i(B^\dagger C - C^\dagger B), \quad L_y^{(i)} = -i(C^\dagger A - A^\dagger C), \quad L_z^{(i)} = -i(A^\dagger B - B^\dagger A). \quad (\text{S8})$$

For later convenience, it is better to introduce the raising, lowering, and orbital angular momentum preserving operators acting on the empty t_{2g} manifold as [S56]

$$\mathcal{D}_{i;0}^\dagger |0\rangle = C_i^\dagger |0\rangle, \quad \mathcal{D}_{i;+}^\dagger |0\rangle = \frac{1}{\sqrt{2}} (A_i^\dagger + iB_i^\dagger) |0\rangle, \quad \mathcal{D}_{i;-}^\dagger |0\rangle = \frac{1}{\sqrt{2}} (A_i^\dagger - iB_i^\dagger) |0\rangle, \quad (\text{S9})$$

where we consider the implicit spin dependence on the operators defined above in Eq. (S7). It is straightforward to check that the states defined above have fixed orbital angular momentum as

$$\langle 0 | \mathcal{D}_{i;0} L_z^{(i)} | \mathcal{D}_{i;0}^\dagger |0\rangle = 0, \quad \langle 0 | \mathcal{D}_{i;+} L_z^{(i)} | \mathcal{D}_{i;+}^\dagger |0\rangle = 1, \quad \langle 0 | \mathcal{D}_{i;-} L_z^{(i)} | \mathcal{D}_{i;-}^\dagger |0\rangle = -1. \quad (\text{S10})$$

Finally, we focus on the effective spin angular momentum states. The effective total spin is $\mathbf{S}_{\text{eff}} = 1$ with the three spin components as $|m_s = 1\rangle$, $|m_s = -1\rangle$, and $m_s = 0$. The first two states are easily written in the \mathcal{D} operator basis

$$\mathcal{D}_{i;\gamma;\uparrow\uparrow}^\dagger |0\rangle, \quad \forall m_s = 1, \quad \mathcal{D}_{i;\gamma;\downarrow\downarrow}^\dagger |0\rangle, \quad \forall m_s = -1 \quad (\gamma = \{0, \pm 1\}), \quad (\text{S11})$$

where \uparrow, \downarrow corresponds to the specific spin-orientation in Eq. (S7), such that for a state with $m_l = 1$, and $m_s = 1$, we can write it as

$$\mathcal{D}_{i;+, \uparrow\uparrow}^\dagger = \frac{1}{\sqrt{2}} (d_{i;xy\uparrow}^\dagger d_{i;zx\uparrow}^\dagger + i d_{i;xy\uparrow}^\dagger d_{i;yz\uparrow}^\dagger) |0\rangle. \quad (\text{S12})$$

The other states can be written in a similar fashion. For latter convenience, we rewrite all the low-lying nine states [see Fig. S1(b)] in the $|m_l, m_s\rangle$ basis as

$$|1, 1\rangle = \frac{1}{\sqrt{2}} (d_{i;xy\uparrow}^\dagger d_{i;zx\uparrow}^\dagger + i d_{i;xy\uparrow}^\dagger d_{i;yz\uparrow}^\dagger) |0\rangle, \quad (\text{S13a})$$

$$|1, 0\rangle = \frac{1}{2} (d_{i;xy\uparrow}^\dagger d_{i;zx\downarrow}^\dagger + d_{i;xy\downarrow}^\dagger d_{i;zx\uparrow}^\dagger + i d_{i;xy\uparrow}^\dagger d_{i;yz\downarrow}^\dagger + i d_{i;xy\downarrow}^\dagger d_{i;yz\uparrow}^\dagger) |0\rangle, \quad (\text{S13b})$$

$$|1, -1\rangle = \frac{1}{\sqrt{2}} (d_{i;xy\downarrow}^\dagger d_{i;zx\downarrow}^\dagger + i d_{i;xy\downarrow}^\dagger d_{i;yz\downarrow}^\dagger) |0\rangle, \quad (\text{S13c})$$

$$|-1, 1\rangle = \frac{1}{\sqrt{2}} (d_{i;xy\uparrow}^\dagger d_{i;zx\uparrow}^\dagger - i d_{i;xy\uparrow}^\dagger d_{i;yz\uparrow}^\dagger) |0\rangle, \quad (\text{S13d})$$

$$|-1, 0\rangle = \frac{1}{2} (d_{i;xy\uparrow}^\dagger d_{i;zx\downarrow}^\dagger + d_{i;xy\downarrow}^\dagger d_{i;zx\uparrow}^\dagger - i d_{i;xy\uparrow}^\dagger d_{i;yz\downarrow}^\dagger - i d_{i;xy\downarrow}^\dagger d_{i;yz\uparrow}^\dagger) |0\rangle, \quad (\text{S13e})$$

$$|-1, -1\rangle = \frac{1}{\sqrt{2}} (d_{i;xy\downarrow}^\dagger d_{i;zx\downarrow}^\dagger - i d_{i;xy\downarrow}^\dagger d_{i;yz\downarrow}^\dagger) |0\rangle, \quad (\text{S13f})$$

$$|0, 1\rangle = d_{i;yz,\uparrow}^\dagger d_{i;zx,\uparrow}^\dagger |0\rangle, \quad (\text{S13g})$$

$$|0, 0\rangle = \frac{1}{\sqrt{2}} (d_{i;yz\uparrow}^\dagger d_{i;zx\downarrow}^\dagger + d_{i;yz\downarrow}^\dagger d_{i;zx\uparrow}^\dagger) |0\rangle, \quad (\text{S13h})$$

$$|0, -1\rangle = d_{i;yz,\downarrow}^\dagger d_{i;zx,\downarrow}^\dagger |0\rangle. \quad (\text{S13i})$$

Note that the SOC is comparable and often exceeds the strength of the Hund's coupling. This subsequently leads to the three different states in the Hund's + SOC submanifold [Eq. (S13a)-Eq. (S13i)] corresponding to $\mathbf{J} = 2$ (pseudo-spin-quintuplet), $\mathbf{J} = 1$ (pseudo-spin-triplet), and $\mathbf{J} = 0$ (pseudo-spin-singlet) sectors [S30]. Finally, the $\mathbf{J} = 2$ states further split into the T_{2g} , and E_g manifold as explained earlier in Eq. (S2).

C. Clebsch-Gordon coefficients: Individual states

Now, we rewrite the atomic singlet, triplet, and quintuplet states (in the \mathbf{J} basis) in terms of the $|m_l, m_s\rangle$ basis utilizing the Clebsch-Gordon coefficients. Consequently, we obtain

$$|\mathbf{J}_i = 0; J_{i;z} = 0\rangle = \frac{1}{\sqrt{3}} (|1, -1\rangle - |0, 0\rangle + |-1, 1\rangle), \quad (\text{S14a})$$

$$|\mathbf{J}_i = 1; J_{i;z} = +1\rangle = \frac{1}{\sqrt{2}} (|1, 0\rangle - |0, 1\rangle), \quad (\text{S14b})$$

$$|\mathbf{J}_i = 1; J_{i;z} = 0\rangle = \frac{1}{\sqrt{2}} (|1, -1\rangle - |-1, 1\rangle), \quad (\text{S14c})$$

$$|\mathbf{J}_i = 1; J_{i;z} = -1\rangle = -\frac{1}{\sqrt{2}} (|-1, 0\rangle - |0, -1\rangle), \quad (\text{S14d})$$

$$|\mathbf{J}_i = 2; J_{i;z} = +2\rangle = |1, 1\rangle, \quad (\text{S14e})$$

$$|\mathbf{J}_i = 2; J_{i;z} = +1\rangle = \frac{1}{\sqrt{2}} (|1, 0\rangle + |0, 1\rangle), \quad (\text{S14f})$$

$$|\mathbf{J}_i = 2; J_{i;z} = 0\rangle = \frac{1}{\sqrt{6}} (|1, -1\rangle + 2|0, 0\rangle + |-1, 1\rangle), \quad (\text{S14g})$$

$$|\mathbf{J}_i = 2; J_{i;z} = -1\rangle = -\frac{1}{\sqrt{2}} (|-1, 0\rangle + |0, -1\rangle), \quad (\text{S14h})$$

$$|\mathbf{J}_i = 2; J_{i;z} = -2\rangle = |-1, -1\rangle. \quad (\text{S14i})$$

Focusing on the energy splitting as shown in Fig. S1(b) as discussed earlier, the lowest doublet E_g can be written explicitly with the above states as

$$|E_g\rangle: \quad |\uparrow\rangle = \frac{|\mathbf{J}_i = 2; J_{i;z} = +2\rangle + |\mathbf{J}_i = 2; J_{i;z} = -2\rangle}{\sqrt{2}}, \quad |\downarrow\rangle = |\mathbf{J}_i = 2; J_{i;z} = 0\rangle. \quad (\text{S15})$$

Using the two-electron states in Eq. (S13a), Eq. (S13f), and Eq. (S13h) in Eq. (S15), one can obtain the doublet states as in Eq. (1) of the main text. Note that the above two pseudo-spin states are non-Kramer's doublet. In terms of the original spin-orbit coupled d -electron operators, the above two pseudo-spin states are written as

$$|i; \uparrow\rangle = \frac{1}{2} (d_{i;xy\uparrow}^\dagger d_{i;zx\uparrow}^\dagger + d_{i;xy\downarrow}^\dagger d_{i;zx\downarrow}^\dagger + id_{i;xy\uparrow}^\dagger d_{i;yz\uparrow}^\dagger - id_{i;xy\downarrow}^\dagger d_{i;yz\downarrow}^\dagger) |0\rangle, \quad (\text{S16a})$$

$$|i; \downarrow\rangle = \frac{1}{2\sqrt{3}} (d_{i;xy\downarrow}^\dagger d_{i;zx\downarrow}^\dagger + d_{i;xy\uparrow}^\dagger d_{i;zx\uparrow}^\dagger + 2d_{i;yz\uparrow}^\dagger d_{i;zx\downarrow}^\dagger + 2d_{i;yz\downarrow}^\dagger d_{i;zx\uparrow}^\dagger + id_{i;xy\downarrow}^\dagger d_{i;yz\downarrow}^\dagger - id_{i;xy\uparrow}^\dagger d_{i;yz\uparrow}^\dagger) |0\rangle. \quad (\text{S16b})$$

II. SCHRIEFFER-WOLFF TRANSFORMATION: MULTIPOLAR EXCHANGE HAMILTONIAN

In the previous section, we described the origin of low-energy effective pseudo-spin [non-Kramer's doublet, E_g] in the atomic limit of each TM atom. However, there will always be virtual electron transfer between the neighboring TM sites in a TM compound. Such virtual exchanges lead to an effective interaction between the emergent pseudo-spin states. Before addressing the emergence of such an exchange interaction, we first notice that the two non-Kramer's states in Eq. (S15) host the non-vanishing expectation value of certain higher-order operators (multipolar). It is easy to see that only three Stevens operators can have non-vanishing expectation values within these low-energy states. We define these higher-order (multipolar) moments as [S57]

$$\mathcal{O}_{20} = 3J_z^2 - \mathbf{J}^2, \quad \mathcal{O}_{22} = J_x^2 - J_y^2, \quad \mathsf{T}_{xyz} = \overline{J_x J_y J_z}. \quad (\text{S17})$$

Note that the first two operators are quadrupolar, and the last one is an octupolar moment (the overline signifies the full symmetrization over the directions $\{x, y, z\}$). The low-energy ground states are manifestly dipole inactive. It is easy to check that the above operators have finite expectation values between the pseudo-spin up and down states as

$$\langle i; \uparrow | \mathcal{O}_{20} | i; \uparrow \rangle = 6, \quad \langle i; \downarrow | \mathcal{O}_{20} | i; \downarrow \rangle = -6, \quad (\text{S18a})$$

$$\langle i; \uparrow | \mathcal{O}_{22} | i; \downarrow \rangle = 2\sqrt{3}, \quad \langle i; \downarrow | \mathcal{O}_{22} | i; \uparrow \rangle = 2\sqrt{3}, \quad (\text{S18b})$$

$$\langle i; \uparrow | \mathbb{T}_{xyz} | i; \downarrow \rangle = -i\sqrt{3}, \quad \langle i; \downarrow | \mathbb{T}_{xyz} | i; \uparrow \rangle = i\sqrt{3}. \quad (\text{S18c})$$

Upon suitable renormalization, we map the three Stevens operators to $\text{SU}(2)$ generators by considering the standard Pauli matrices as $(\tilde{\sigma}^x, \tilde{\sigma}^y, \tilde{\sigma}^z)$. The normalization becomes evident from the above relations as

$$\frac{\mathcal{O}_{22}}{4\sqrt{3}} \rightarrow \tilde{\sigma}^x, \quad \frac{\mathbb{T}_{xyz}}{2\sqrt{3}} \rightarrow \tilde{\sigma}^y, \quad \frac{\mathcal{O}_{20}}{12} \rightarrow \tilde{\sigma}^z. \quad (\text{S19})$$

However, these pseudo-spin generators are distinct from the conventional spin- $\frac{1}{2}$ representation. Most importantly, the transformation property under time-reversal symmetry (TRS) transformation (\mathcal{T}) is distinct, as is evident from the form of the multipolar moments, and we obtain

$$\mathcal{T} : \{\tilde{\sigma}^x, \tilde{\sigma}^y, \tilde{\sigma}^z\} \rightarrow \{\tilde{\sigma}^x, -\tilde{\sigma}^y, \tilde{\sigma}^z\}. \quad (\text{S20})$$

A. Derivation of the low-energy effective exchange interaction

Up to this point, we have described the low-energy behavior of the multipolar degrees of freedom at each site. However, due to the virtual exchange of electrons, these individual multipolar moments develop couplings with neighboring sites. The Schrieffer-Wolff transformation (SWT) is a powerful tool that systematically derives a low-energy exchange Hamiltonian that captures these couplings. Interested readers can refer to Refs. [S58, S59] for a more detailed explanation of SWT. However, for a self-contained analysis, we will concisely describe SWT. We begin with the total Hamiltonian $\mathcal{H} = \mathcal{H}_0 + \mathcal{H}_1$, where \mathcal{H}_0 typically represents the correlated part, and \mathcal{H}_1 is considered a small perturbation. We then perform a unitary transformation as follows

$$\begin{aligned} \mathcal{H}' &= U^\dagger \mathcal{H} U = e^{i\mathcal{S}} \mathcal{H} e^{-i\mathcal{S}}, \quad (\text{S21}) \\ &= \mathcal{H} + [i\mathcal{S}, \mathcal{H}] + \frac{1}{2!} [i\mathcal{S}, [i\mathcal{S}, \mathcal{H}]] + \frac{1}{3!} [i\mathcal{S}, [i\mathcal{S}, [i\mathcal{S}, \mathcal{H}]]] + \dots, \\ &= \mathcal{H}_0 + \mathcal{H}_1 + i[\mathcal{S}, \mathcal{H}_0] + i[\mathcal{S}, \mathcal{H}_1] - \frac{1}{2} [\mathcal{S}, [\mathcal{S}, \mathcal{H}_0]] - \frac{1}{2} [\mathcal{S}, [\mathcal{S}, \mathcal{H}_1]] - \frac{i}{3!} [\mathcal{S}, [\mathcal{S}, [\mathcal{S}, \mathcal{H}_0]]] - \frac{i}{3!} [\mathcal{S}, [\mathcal{S}, [\mathcal{S}, \mathcal{H}_1]]] + \dots, \end{aligned}$$

where \mathcal{S} is a hermitian operator. We now write the generator \mathcal{S} in a perturbative expansion with the hopping parameters as $\mathcal{S} = \mathcal{S}^{(1)} + \mathcal{S}^{(2)} + \mathcal{S}^{(3)} + \mathcal{S}^{(4)} + \dots$. Now, plugging this back in Eq. (S20) and collecting terms of the same order in expansion, we obtain

$$\begin{aligned} \mathcal{H}' &= \mathcal{H}_0 + \mathcal{H}_1 + i[\mathcal{S}^{(1)}, \mathcal{H}_0] \\ &+ i[\mathcal{S}^{(1)}, \mathcal{H}_1] + i[\mathcal{S}^{(2)}, \mathcal{H}_0] - \frac{1}{2} [\mathcal{S}^{(1)}, [\mathcal{S}^{(1)}, \mathcal{H}_0]] \\ &+ i[\mathcal{S}^{(3)}, \mathcal{H}_0] + i[\mathcal{S}^{(2)}, \mathcal{H}_1] - \frac{1}{2} [\mathcal{S}^{(1)}, [\mathcal{S}^{(1)}, \mathcal{H}_1] + [\mathcal{S}^{(2)}, \mathcal{H}_0]] - \frac{1}{2} [\mathcal{S}^{(2)}, [\mathcal{S}^{(1)}, \mathcal{H}_0]] - \frac{i}{3!} [\mathcal{S}^{(1)}, [\mathcal{S}^{(1)}, [\mathcal{S}^{(1)}, \mathcal{H}_0]]] \\ &+ i[\mathcal{S}^{(4)}, \mathcal{H}_0] + i[\mathcal{S}^{(3)}, \mathcal{H}_1] - \frac{1}{2} [\mathcal{S}^{(3)}, [\mathcal{S}^{(1)}, \mathcal{H}_0]] - \frac{1}{2} [\mathcal{S}^{(2)}, [\mathcal{S}^{(1)}, \mathcal{H}_1] + [\mathcal{S}^{(2)}, \mathcal{H}_0]] - \frac{1}{2} [\mathcal{S}^{(1)}, [\mathcal{S}^{(2)}, \mathcal{H}_1] + [\mathcal{S}^{(3)}, \mathcal{H}_0]] \\ &- \frac{i}{3!} [\mathcal{S}^{(1)}, [\mathcal{S}^{(1)}, [\mathcal{S}^{(1)}, \mathcal{H}_1]] + [\mathcal{S}^{(1)}, [\mathcal{S}^{(2)}, \mathcal{H}_0]] + [\mathcal{S}^{(2)}, [\mathcal{S}^{(1)}, \mathcal{H}_0]]] - \frac{i}{3!} [\mathcal{S}^{(2)}, [\mathcal{S}^{(1)}, [\mathcal{S}^{(1)}, \mathcal{H}_0]]] \\ &+ \frac{1}{4!} [\mathcal{S}^{(1)}, [\mathcal{S}^{(1)}, [\mathcal{S}^{(1)}, [\mathcal{S}^{(1)}, \mathcal{H}_0]]]] + \mathcal{O}(S^{(5)}) \dots \end{aligned} \quad (\text{S22})$$

The evaluation of the effective Hamiltonian at each perturbative order becomes evident from Eq. (S21). We focus on the terms up to the n -th order and obtain the low-energy effective Hamiltonians up to the $(n+1)$ -th order, along with the corresponding generating functions $\mathcal{S}^{(n)}$. Here, we restrict ourselves to the generic expressions for the first two lowest-order effective Hamiltonians below. These will be utilized later to derive the multipolar exchange Hamiltonians. However, for the explicit evaluation of the generating functions $\mathcal{S}^{(n)}$ at each order, we need to

introduce the projection operators \mathcal{P} and \mathcal{Q} . These operators act on the low- and high-energy sectors of the total Hilbert space, respectively.

Second-order effective Hamiltonian – The Hamiltonian can be determined up to the second order in perturbation parameters by utilizing Eq. (S21) (assuming $\mathcal{S}^{(2)} = 0$), and it is given by

$$\mathcal{H}_{\text{eff}}^{(2)} = \frac{i}{2} [\mathcal{S}^{(1)}, \mathcal{H}_1]. \quad (\text{S23})$$

The dynamic equation governing the generating function $\mathcal{S}^{(1)}$ can be derived from the first-order terms in Eq. (S21), leading to

$$[\mathcal{S}^{(1)}, \mathcal{H}_0] = i\mathcal{H}_1. \quad (\text{S24})$$

The equation presented above is a matrix equation, where $\mathcal{S}^{(1)}$ is a 2×2 matrix defined within the space of projectors \mathcal{P} and \mathcal{Q} , and can be expressed as

$$\mathcal{S}^{(1)} = \begin{pmatrix} \mathcal{P}\mathcal{S}^{(1)}\mathcal{P} & \mathcal{P}\mathcal{S}^{(1)}\mathcal{Q} \\ \mathcal{Q}\mathcal{S}^{(1)}\mathcal{P} & \mathcal{Q}\mathcal{S}^{(1)}\mathcal{Q} \end{pmatrix}. \quad (\text{S25})$$

As we are primarily concerned with the low-energy states, the diagonal elements are set to zero, and our focus is solely on solving for the off-diagonal elements. This leads us to the following equation (it is important to note that \mathcal{H}_0 is diagonal in the \mathcal{Q} space):

$$\begin{aligned} \mathcal{P}\mathcal{S}^{(1)}\mathcal{H}_0\mathcal{Q} - \mathcal{P}\mathcal{H}_0\mathcal{S}^{(1)}\mathcal{Q} &= i\mathcal{P}\mathcal{H}_1\mathcal{Q} \\ \mathcal{P}\mathcal{S}^{(1)}\mathcal{Q}\mathcal{Q}\mathcal{H}_0\mathcal{Q} - \mathcal{P}\mathcal{H}_0\mathcal{Q}\mathcal{Q}\mathcal{S}^{(1)}\mathcal{Q} &= i\mathcal{P}\mathcal{H}_1\mathcal{Q} \end{aligned} \quad (\text{S26a})$$

$$\begin{aligned} \mathcal{Q}\mathcal{S}^{(1)}\mathcal{H}_0\mathcal{P} - \mathcal{Q}\mathcal{H}_0\mathcal{S}^{(1)}\mathcal{P} &= i\mathcal{Q}\mathcal{H}_1\mathcal{P} \\ \mathcal{Q}\mathcal{S}^{(1)}\mathcal{Q}\mathcal{Q}\mathcal{H}_0\mathcal{P} - \mathcal{Q}\mathcal{H}_0\mathcal{Q}\mathcal{Q}\mathcal{S}^{(1)}\mathcal{P} &= i\mathcal{Q}\mathcal{H}_1\mathcal{P}, \end{aligned} \quad (\text{S26b})$$

where $\mathcal{Q}\mathcal{H}_0\mathcal{Q}$ corresponds to eigenvalues in the intermediate high-energy states.

Third-order effective Hamiltonian – Indeed, let us also outline the steps for obtaining the third-order extension. Starting from Eq. (S21), we can systematically derive the effective Hamiltonian within the framework of third-order perturbation theory. We examine the algebraic and dynamical equation for the generating function $\mathcal{S}^{(2)}$ as

$$[\mathcal{S}^{(2)}, \mathcal{H}_0] = -[\mathcal{S}^{(1)}, \mathcal{H}_1]. \quad (\text{S27})$$

Note that we can simplify the last term in the second-order expansion of Eq. (S21) using the expression for $\mathcal{S}^{(1)}$ from Eq. (S23) as follows. Consequently, the effective Hamiltonian up to third-order in perturbation becomes (assuming $\mathcal{S}^{(3)} = 0$ as before):

$$\mathcal{H}_{\text{eff}}^{(3)} = \frac{i}{2} [\mathcal{S}^{(2)}, \mathcal{H}_1] + \frac{1}{6} [\mathcal{S}^{(1)}, [\mathcal{S}^{(1)}, \mathcal{H}_1]]. \quad (\text{S28})$$

Using the projector-based decomposition, we can continue with the algebraic equations of motion for the elements of the generating function $\mathcal{S}^{(2)}$. They are given by

$$\begin{aligned} \mathcal{P}\mathcal{S}^{(2)}\mathcal{Q}\mathcal{Q}\mathcal{H}_0\mathcal{Q} - \mathcal{P}\mathcal{H}_0\mathcal{Q}\mathcal{Q}\mathcal{S}^{(2)}\mathcal{Q} &= \mathcal{P}\mathcal{H}_1\mathcal{Q}\mathcal{Q}\mathcal{S}^{(1)}\mathcal{Q} - \mathcal{P}\mathcal{S}^{(1)}\mathcal{Q}\mathcal{Q}\mathcal{H}_1\mathcal{Q} \\ &\Rightarrow \mathcal{P}\mathcal{S}^{(2)}\mathcal{Q}\mathcal{Q}\mathcal{H}_0\mathcal{Q} = -\mathcal{P}\mathcal{S}^{(1)}\mathcal{Q}\mathcal{Q}\mathcal{H}_1\mathcal{Q}, \end{aligned} \quad (\text{S29a})$$

$$\begin{aligned} \mathcal{Q}\mathcal{S}^{(2)}\mathcal{Q}\mathcal{Q}\mathcal{H}_0\mathcal{P} - \mathcal{Q}\mathcal{H}_0\mathcal{Q}\mathcal{Q}\mathcal{S}^{(2)}\mathcal{P} &= \mathcal{Q}\mathcal{H}_1\mathcal{Q}\mathcal{Q}\mathcal{S}^{(1)}\mathcal{P} - \mathcal{Q}\mathcal{S}^{(1)}\mathcal{Q}\mathcal{Q}\mathcal{H}_1\mathcal{P} \\ &\Rightarrow \mathcal{Q}\mathcal{H}_0\mathcal{Q}\mathcal{Q}\mathcal{S}^{(2)}\mathcal{P} = -\mathcal{Q}\mathcal{H}_1\mathcal{Q}\mathcal{Q}\mathcal{S}^{(1)}\mathcal{P}. \end{aligned} \quad (\text{S29b})$$

B. Second-order multipolar exchange interaction

We can now compute the effective low-energy multipolar exchange interaction in edge-sharing octahedral configurations. In the context of octahedral environments, it is essential to consider the anisotropic nature of the Slater-Koster

hopping parameters between neighboring sites. For the analysis, we will focus on a specific bond connecting two neighboring TM ions, which we will label as the z -bond aligned in the xy -plane. Similar analyses can be carried out for the exchange interactions along other bonds by applying the appropriate rotations. First, we consider the perturbative hopping Hamiltonian along the z -bond as

$$\mathcal{H}_1 = -t_2 \sum_{\langle ij \rangle; \sigma} (d_{i;yz\sigma}^\dagger d_{j;zx\sigma} + d_{i;zx\sigma}^\dagger d_{j;yz\sigma}) + \text{h.c.}, \quad (\text{S30})$$

where t_2 is the nearest-neighbor (NN) hopping amplitude. We now follow Eq. (S23) to write the effective Hamiltonian in the second order as ($\mathcal{P}_{\text{low}} = \mathcal{P}_i \mathcal{P}_j$ is the product of the low-energy projection operators in two sites)

$$\begin{aligned} & \mathcal{P}_{\text{low}} \mathcal{H}_{\text{eff}}^{(2)} \mathcal{P}_{\text{low}} \\ &= -\frac{1}{2\mathcal{Q}_j \mathcal{H}_0^{(j)} \mathcal{Q}_j} \mathcal{P}_i \mathcal{H}_1 \mathcal{Q}_j \mathcal{Q}_j \mathcal{H}_1 \mathcal{P}_i + i \leftrightarrow j + \text{h.c.}, \\ &= -\frac{t_2^2}{2} \sum_{\substack{\{n_i, n_l\} \\ \alpha\beta}} \frac{\langle i, n_1; j, n_2 | d_{i;\beta\sigma}^\dagger d_{j;\alpha\sigma} | \psi_{i, \eta_1}; \phi_{j, \eta_2} \rangle \langle \psi_{i, \eta_1}; \phi_{j, \eta_2} | d_{j;\alpha\sigma}^\dagger d_{i;\beta\sigma} | i, n_3; j, n_4 \rangle}{\Delta E_{\text{ex}}^{\{n_i, \eta_i\}}} |i, n_1; j, n_2\rangle \langle i, n_3; j, n_4| + i \leftrightarrow j + \text{h.c.}, \end{aligned} \quad (\text{S31})$$

where $|i, n\rangle \forall n = \uparrow, \downarrow$ corresponds to the ground-state doublets as mentioned in Eq. (S15), $|\psi_{i, \eta}\rangle \forall \eta = \text{A, B, C, D}$ and $|\phi_{i, \eta}\rangle \forall \eta = \text{A, B, C, D}$ corresponds to the three-electron and one-electron intermediate states, respectively. Finally, $\Delta E_{\text{ex}}^{\{n_i, \eta_i\}}$ corresponds to the atomic excitation energy for the virtual process involved. It is computed as [S53]

$$\Delta E_{\text{ex}}^{\{n_i, \eta_i\}} = E^{(i)}(N_i = 3) + E^{(j)}(N_j = 1) - E^{(i)}(N_i = 2) - E^{(j)}(N_j = 2) = U - 3J_{\text{H}} + \lambda. \quad (\text{S32})$$

Note that the virtual hopping between the TM atoms changes the electron filling in the intermediate states as

$$d_i^2 d_j^2 \rightarrow d_i^3 d_j^1 \rightarrow d_i^2 d_j^2 + i \leftrightarrow j. \quad (\text{S33})$$

For latter reference, we provide the expressions for the intermediate one- and three-electron ground states within the octahedral environment, ordered by their hierarchical energy distribution as previously outlined. These states are defined as follows [S53, S54]

$$|\psi_{i, \text{A}}\rangle = d_{i;xy\uparrow}^\dagger d_{i;yz\uparrow}^\dagger d_{i;zx\uparrow}^\dagger |0\rangle, \quad (\text{S34a})$$

$$|\psi_{i, \text{B}}\rangle = d_{i;xy\downarrow}^\dagger d_{i;yz\downarrow}^\dagger d_{i;zx\downarrow}^\dagger |0\rangle, \quad (\text{S34b})$$

$$|\psi_{i, \text{C}}\rangle = \frac{1}{\sqrt{3}} (d_{i;xy\uparrow}^\dagger d_{i;yz\uparrow}^\dagger d_{i;zx\downarrow}^\dagger + d_{i;xy\uparrow}^\dagger d_{i;yz\downarrow}^\dagger d_{i;zx\uparrow}^\dagger + d_{i;xy\downarrow}^\dagger d_{i;yz\uparrow}^\dagger d_{i;zx\uparrow}^\dagger) |0\rangle, \quad (\text{S34c})$$

$$|\psi_{i, \text{D}}\rangle = \frac{1}{\sqrt{3}} (d_{i;xy\downarrow}^\dagger d_{i;yz\downarrow}^\dagger d_{i;zx\uparrow}^\dagger + d_{i;xy\downarrow}^\dagger d_{i;yz\uparrow}^\dagger d_{i;zx\downarrow}^\dagger + d_{i;xy\uparrow}^\dagger d_{i;yz\downarrow}^\dagger d_{i;zx\downarrow}^\dagger) |0\rangle, \quad (\text{S34d})$$

$$|\phi_{i, \text{A}}\rangle = \frac{1}{\sqrt{2}} (d_{i;yz, \uparrow}^\dagger + i d_{i;zx, \uparrow}^\dagger) |0\rangle, \quad (\text{S34e})$$

$$|\phi_{i, \text{B}}\rangle = \frac{1}{\sqrt{2}} (d_{i;yz, \downarrow}^\dagger - i d_{i;zx, \downarrow}^\dagger) |0\rangle, \quad (\text{S34f})$$

$$|\phi_{i, \text{C}}\rangle = \sqrt{\frac{2}{3}} \left(d_{i;xy, \uparrow}^\dagger - \frac{d_{i;yz, \downarrow}^\dagger + i d_{i;zx, \downarrow}^\dagger}{2} \right) |0\rangle, \quad (\text{S34g})$$

$$|\phi_{i, \text{D}}\rangle = \sqrt{\frac{2}{3}} \left(d_{i;xy, \downarrow}^\dagger + \frac{d_{i;yz, \uparrow}^\dagger - i d_{i;zx, \uparrow}^\dagger}{2} \right) |0\rangle, \quad (\text{S34h})$$

where $|0\rangle$ corresponds to the empty t_{2g} states. We do not consider the e_g states explicitly, assuming the crystal field remains large in the intermediate states. In the case of d^3 -electronic configuration, there are three electrons in t_{2g} , and in the presence of Hund's coupling, the total orbital angular momentum is completely quenched. Consequently, the SOC is effectively absent in this case. We define new composite operators $b_{i\tilde{\sigma}}^\dagger \forall \tilde{\sigma} = \uparrow, \downarrow$ which create two non-Kramer's states in Eq. (S15) as

$$b_{i\uparrow}^\dagger |0\rangle = |i, \uparrow\rangle, \quad b_{i\downarrow}^\dagger |0\rangle = |i, \downarrow\rangle, \quad (\text{S35})$$

TABLE I. The summary of the transformation of various quantities under the irreducible representations of the dihedral group D_{4h} [S61]. This transformation applies to the edge-sharing geometry.

Object	S_{4z}	C_3	\mathcal{T}
x	$-y$	y	x
y	x	z	y
z	$-z$	x	z
$\tilde{\sigma}^x$	$\tilde{\sigma}^x$	$-\frac{1}{2}\tilde{\sigma}^x - \frac{\sqrt{3}}{2}\tilde{\sigma}^z$	$\tilde{\sigma}^x$
$\tilde{\sigma}^y$	$-\tilde{\sigma}^y$	$\tilde{\sigma}^y$	$-\tilde{\sigma}^y$
$\tilde{\sigma}^z$	$-\tilde{\sigma}^z$	$\frac{\sqrt{3}}{2}\tilde{\sigma}^x - \frac{1}{2}\tilde{\sigma}^z$	$\tilde{\sigma}^z$

and introduce the pseudo-SU(2) generating functions with them as

$$\tilde{\sigma}_i = b_{i\alpha}^\dagger \boldsymbol{\tau}_{\alpha\beta} b_{i\beta}, \quad (\text{S36})$$

where $\boldsymbol{\tau} = (\tau_x, \tau_y, \tau_z)$ is the vector of Pauli matrices. In this way, we compute all the matrix elements in Eq. (S30) using DiracQ package in MATHEMATICA V.14.1 [S60], and subsequently rewrite the resulting expressions in the pseudo-spin operators ($\tilde{\sigma}^x, \tilde{\sigma}^y, \tilde{\sigma}^z$).

In this context, the hopping mechanism is characterized by non-conservation of orbital properties, as indicated in Eq. (S30). Before proceeding further, we explore the transformations of multipolar operators under the dihedral group generators, specifically S_{4z} and C_3 rotations around the (111) axis for the edge-sharing geometry. The corresponding transformations are outlined in Table I. Adhering to these symmetry constraints, we derive a second-order Hamiltonian that aligns with previous theoretical studies [S32, S33, S37, S52]. In the absence of Hund's coupling and spin-orbit coupling (SOC) effects in the intermediate states, and considering all 120 intermediate states (${}^6C_1 \times {}^6C_3$), resulting from combinations of d^1 and d^3 electronic configurations, the effective low-energy multipolar exchange Hamiltonian exhibits a distinctive bond-independent character as

$$\mathcal{H}_{\text{eff}}^{(0)} = \mathcal{H}_x^{(0)} + \mathcal{H}_y^{(0)} + \mathcal{H}_z^{(0)}, \quad (\text{S37a})$$

$$\mathcal{H}_\eta^{(0)} = \frac{2t_2^2}{3\Delta E_{\text{ex.}}} \sum_{(ij),z} (\tilde{\sigma}_i^y \tilde{\sigma}_j^y - \tilde{\sigma}_i^x \tilde{\sigma}_j^x - \tilde{\sigma}_i^z \tilde{\sigma}_j^z), \quad \eta \in \{x, y, z\}. \quad (\text{S37b})$$

The multipolar exchange Hamiltonian takes an isotropic and bond-independent form, as articulated in Eq. (S37a)-(S37b). The bilinear exchange form closely resembles the bond-dependent Kugel-Khomskii orbital exchange model [S42]. We further note that the cubic rotation symmetry along the [111] direction constrains the quadrupolar exchange interaction to be invariant under $C_{[111]}^3$ rotation (see Table. I). Note that for x and y -bonds the pseudo-spin up and down states in Eq. (S16a), and Eq. (S16b) are rotated accordingly so that the transformed $\tilde{\sigma}^z$ is along the projected octahedral x and y -axis on the [111] plane.

C. Third-order multipolar exchange interaction

In this section, we derive the third-order expression for the low-energy effective Hamiltonian between the multipolar degrees of freedom. Utilizing the dynamical equations for the generator $\mathcal{S}^{(2)}$ in Eq. (S29a)-Eq. (S29b), we obtain the effective Hamiltonian from Eq. (S28) as

$$\mathcal{H}_{\text{eff}}^{(3)} = \frac{2t_2^2 t'_2}{3\Delta E_{\text{ex.}}} \sin \frac{e\Phi}{\hbar c} \sum_{\triangle \langle ij k \rangle} \left[\left(\frac{2\tilde{\sigma}_i^z \tilde{\sigma}_j^z \tilde{\sigma}_k^y}{9} + \frac{2\tilde{\sigma}_i^y \tilde{\sigma}_j^z \tilde{\sigma}_k^z}{9} + \frac{2\tilde{\sigma}_i^z \tilde{\sigma}_j^y \tilde{\sigma}_k^z}{9} + \frac{2\tilde{\sigma}_i^x \tilde{\sigma}_j^x \tilde{\sigma}_k^y}{9} + \frac{2\tilde{\sigma}_i^y \tilde{\sigma}_j^x \tilde{\sigma}_k^x}{9} + \frac{2\tilde{\sigma}_i^x \tilde{\sigma}_j^y \tilde{\sigma}_k^x}{9} - \frac{\tilde{\sigma}_i^y \tilde{\sigma}_j^y \tilde{\sigma}_k^y}{9} \right) \right]. \quad (\text{S38})$$

The overlap matrix elements are again computed in DiracQ package in MATHEMATICA V.14.1 [S60]. The trilinear term is only active in the presence of an external magnetic field B . Here, Φ is the total flux enclosed within the triangular plaquette in the presence of B . This is consistent with the C_3 rotations and overall time-reversal symmetry of the system. We incorporate Eq. (S28) to derive the Hamiltonian above. Utilizing the generating functions, the virtual hopping processes can be classified into two types as illustrated in Fig. S2(a,b) – among which only process (a) contributes to the form in Eq. (S38). The contribution from the process in panel (b) of Fig. S2 identically vanishes due to the conservation of J_z angular momentum. In the above derivation the states for three different bond types enter as illustrated in Fig. S2. The pseudo-spin up and pseudo-spin down operators for each bond is rotated in the usual manner as for the E_g doublet as discussed in the main text.

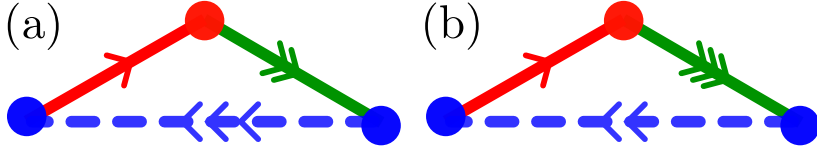


FIG. S2. Two types of the virtual exchange of electrons in the third-order perturbation expansion of the effective Hamiltonian derivation in Eq. (S38). (a) a direct hopping process as illustrated by the arrows, and (b) an indirect hopping in the intermediate states labeled by the arrow. The number of arrows dictates the step of the virtual hopping in the third-order super-exchange process.

III. MULTIPOLAR MULTIFERROICITY

In this section, we provide the details of the derivation leading to Eq. (9) and Eq. (11a)-(11b) in the main text for the ferroelectric polarization and the electrical quadrupolar responses. Motivated by our MC simulation leading to a non-collinear multipolar texture obtained by the exchange Hamiltonian in Eq. (S37a)-(S38), we consider the local approximation of the Hamiltonian as discussed in the main text. The corresponding Hamiltonian is written as

$$\mathcal{H}_0 = -\tilde{U} \sum_i \mathbf{e}_i \cdot \tilde{\boldsymbol{\sigma}}_i, \quad (\text{S39})$$

where $\mathbf{e}_i = (\sin \theta_i \cos \phi_i, \sin \theta_i \sin \phi_i, \cos \theta_i)$, $\tilde{\boldsymbol{\sigma}}_i$ corresponds to the local pseudo-spin at site i , and \tilde{U} corresponds to a phenomenological energy scale (associated with the Hubbard interaction, Hund's coupling strength, SOC and the local crystal field). Now, we rewrite the $|\text{E}_g\rangle$ states in terms of the two d -orbital operators for simplicity as

$$|i; \uparrow\rangle = \left(\frac{d_{i;xy\uparrow}^\dagger d_{i;zx\uparrow}^\dagger}{2} + \frac{d_{i;xy\downarrow}^\dagger d_{i;zx\downarrow}^\dagger}{2} + \frac{id_{i;xy\uparrow}^\dagger d_{i;yz\uparrow}^\dagger}{2} - \frac{id_{i;xy\downarrow}^\dagger d_{i;yz\downarrow}^\dagger}{2} \right) |0\rangle, \quad (\text{S40a})$$

$$|i; \downarrow\rangle = \left(\frac{d_{i;xy\downarrow}^\dagger d_{i;zx\downarrow}^\dagger}{2\sqrt{3}} + \frac{d_{i;xy\uparrow}^\dagger d_{i;zx\uparrow}^\dagger}{2\sqrt{3}} + \frac{d_{i;yz\uparrow}^\dagger d_{i;zx\downarrow}^\dagger}{\sqrt{3}} + \frac{d_{i;yz\downarrow}^\dagger d_{i;zx\uparrow}^\dagger}{\sqrt{3}} + \frac{id_{i;xy\downarrow}^\dagger d_{i;yz\downarrow}^\dagger}{2\sqrt{3}} - \frac{id_{i;xy\uparrow}^\dagger d_{i;yz\uparrow}^\dagger}{2\sqrt{3}} \right) |0\rangle, \quad (\text{S40b})$$

where $|0\rangle$ is the empty t_{2g} -sector. Adopting the Pauli matrix structure, the Hamiltonian in Eq. (S39) can be diagonalized to obtain the eigenfunctions as

$$|\psi_i^+\rangle = \sin \frac{\theta_i}{2} |i; \uparrow\rangle + e^{i\phi_i} \cos \frac{\theta_i}{2} |i; \downarrow\rangle, \quad (\text{S41a})$$

$$|\psi_i^-\rangle = \cos \frac{\theta_i}{2} |i; \uparrow\rangle - e^{i\phi_i} \sin \frac{\theta_i}{2} |i; \downarrow\rangle. \quad (\text{S41b})$$

Here, $|\psi^+\rangle$ is the ground state with energy $-\tilde{U}$, and $|\psi^-\rangle$ is the excited state with energy $+\tilde{U}$. Considering the ground state as $|\psi^+\rangle$, we now consider two different ligand-TM hopping processes to derive the multipolar charge responses. The ligand-TM hopping is written as

$$\mathcal{H}_{\text{hop}} = t_{pd}^\pi d_{i;zx\sigma}^\dagger p_{l';z\sigma} + t_{pd}^\pi d_{i;yz\sigma}^\dagger p_{l';z\sigma} - t_{pd}^\pi d_{j;zx\sigma}^\dagger p_{l';z\sigma} - t_{pd}^\pi d_{j;yz\sigma}^\dagger p_{l';z\sigma} + \text{h.c.}, \quad (\text{S42})$$

where l (l') corresponds to the upper (lower) ligand sites in Fig. S3 and Fig. S4.

A. Ferroelectric polarization

We consider a four-site cluster with two TM and two ligand sites. In the stoichiometric configuration of the TM compound, we consider filled ligand sites with electrons. For subsequent analysis, we rewrite Eq. (S41a) in the following manner as

$$|\psi_i^+\rangle = c_i \underbrace{(|xy \uparrow\rangle_i |zx \uparrow\rangle_i + |xy \downarrow\rangle_i |zx \downarrow\rangle_i)}_{yz} + id_i \underbrace{(|xy \uparrow\rangle_i |yz \uparrow\rangle_i - |xy \downarrow\rangle_i |yz \downarrow\rangle_i)}_{zx} + a_i \underbrace{(|yz \uparrow\rangle_i |zx \downarrow\rangle_i + |yz \downarrow\rangle_i |zx \uparrow\rangle_i)}_{xy}, \quad (\text{S43})$$

where

$$c_i = \frac{\sqrt{3} \sin \frac{\theta_i}{2} + e^{i\phi_i} \cos \frac{\theta_i}{2}}{2\sqrt{3}}, \quad d_i = \frac{\sqrt{3} \sin \frac{\theta_i}{2} - e^{i\phi_i} \cos \frac{\theta_i}{2}}{2\sqrt{3}}, \quad a_i = c_i - d_i,$$

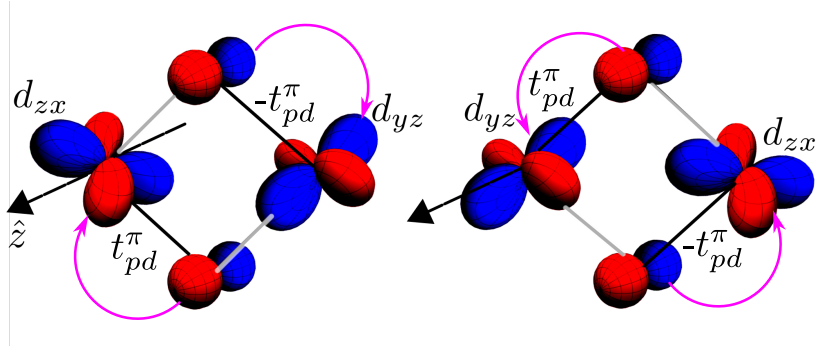


FIG. S3. The virtual hopping of electrons from a filled ligand site to a TM site along the z -bond orientation in the edge-shared geometry. The hopping amplitudes differ in sign between the upper and lower triangles in the TM-ligand-TM clusters.

and we underlined the effective spatial structure of the two-electron composite states in Eq. (S42). We now consider virtual charge transfer between the ligand and the TM atoms within a double exchange framework. The associated paths are shown in Fig. S3. Furthermore, we consider the strong Hund's coupling in the intermediate configuration of d^3, p_z^1, p_z^1 . The corresponding atomic states for a d^3 ion in an octahedral crystal field and Hund's coupling are provided previously in Eq. (S34a)-Eq. (S34d). Now, using these states and the four-site cluster as shown in Fig. S3, we perform a first-order perturbation theory to compute the correction to the ground states in Eq. (S41a). The latter is obtained as

$$\begin{aligned}
 |\psi\rangle = \frac{1}{N} & \left[|\psi_i^+\rangle + |\psi_j^+\rangle + \frac{t_{pd}^{\pi}}{\Delta_{\text{crys.}}} id_i (|xy \uparrow\rangle_i |yz \uparrow\rangle_i |zx\sigma\rangle_i |p_z\rangle_{l'} - |xy \downarrow\rangle_i |yz \downarrow\rangle_i |zx\sigma\rangle_i |p_z\rangle_{l'}) \right. \\
 & - \frac{t_{pd}^{\pi}}{\Delta_{\text{crys.}}} id_j (|xy \uparrow\rangle_j |yz \uparrow\rangle_j |zx\sigma\rangle_j |p_z\rangle_l - |xy \downarrow\rangle_j |yz \downarrow\rangle_j |zx\sigma\rangle_j |p_z\rangle_l) \\
 & + \frac{t_{pd}^{\pi}}{\Delta_{\text{crys.}}} c_i (|xy \uparrow\rangle_i |zx \uparrow\rangle_i |yz\sigma\rangle_i |p_z\rangle_l + |xy \downarrow\rangle_i |zx \downarrow\rangle_i |yz\sigma\rangle_i |p_z\rangle_l) \\
 & \left. - \frac{t_{pd}^{\pi}}{\Delta_{\text{crys.}}} c_j (|xy \uparrow\rangle_j |zx \uparrow\rangle_j |yz\sigma\rangle_j |p_z\rangle_{l'} + |xy \downarrow\rangle_j |zx \downarrow\rangle_j |yz\sigma\rangle_j |p_z\rangle_{l'}) \right], \quad (\text{S44})
 \end{aligned}$$

where N is the normalization factor, $\Delta_{\text{crys.}}$ is the charge-transfer energy between TM d and ligand p orbitals, and l (l') corresponds to the upper (lower) ligand sites in Fig. S3.

Now, in the perturbed state $|\psi\rangle$, we compute the expectation value of the polarization operator $\mathbf{P} = e\mathbf{r}$. Using the parity of the associated states in Eq. (S41a) and Eq. (S43), we notice that only x component of the polarization survives upon evaluating the overlap integrals in $\langle\psi|\mathbf{r}|\psi\rangle$. The polarization for the other bonds can be analogously obtained by using appropriate perturbed states upon different ligand-TM hoppings.

B. Electrical quadrupolar distribution

Here, we provide the details of the derivation for the electrical quadrupole in Eq. (11a)-(11b) in the main text. In this case, we consider the similar four-site cluster but only assume empty ligand sites, and subsequently consider a co-tunneling of two electrons to the upper and lower ligand sites. The co-tunneling could happen from both the left and the right TM sites as shown in Fig. S4. The perturbation calculations are performed exactly similar to the polarization in the previous section. In this case, the co-tunneling induced correction to the ground states is obtained using first-order perturbation theory as

$$|\psi\rangle = \frac{1}{N} \left[|\psi_i^+\rangle + |\psi_j^+\rangle + \left(\frac{t_{pd}^{\pi}}{\Delta_{\text{crys.}}} \right)^2 (2a_i + 2a_j) (|p_z \uparrow\rangle_l |p_z \downarrow\rangle_{l'} + |p_z \downarrow\rangle_l |p_z \uparrow\rangle_{l'}) \right]. \quad (\text{S45})$$

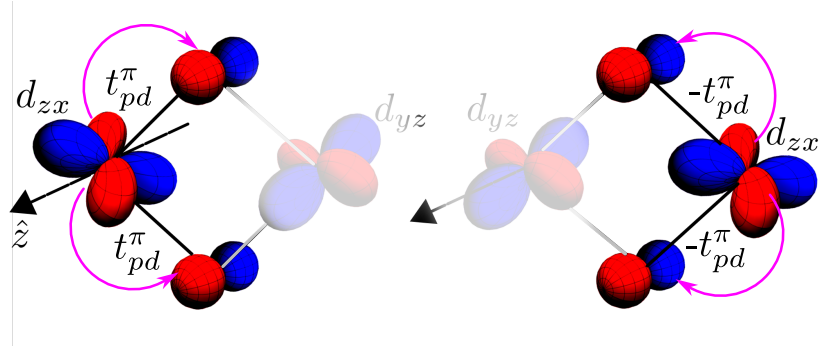


FIG. S4. The virtual hopping of electrons to an empty ligand site from a TM site along the z -bond orientation in the edge-shared geometry. The hopping amplitudes differ in sign between the left and right triangles in the TM-ligand-TM clusters.